Scuola Normale Superiore di Pisa

Classe di Scienze

Ph. D. Thesis

Tomography and manipulation of quantum Hall edge channels

Nicola Paradiso

Advisors:

Prof. Fabio Beltram

Dr. Stefan Heun

2012

To Marco and Giulia

Contents

Introduction

The revolutionary impact of quantum theory is intimately linked to the success of microelectronics. In turn, the ability to exploit quantum effects in nanoscopic devices was often related to the advent of technological breakthroughs (new materials, innovative experimental setup, etc.) that allowed to reveal and control non-classical phenomena. The progress of quantum Hall (QH) physics is a good example of such processes. Initially, the developement of the MBE technique made it possible to grow clean crystals with accurate composition control to the layer-by-layer limit. Hence, it became possible to obtain heterostructures embedding two dimensional electron gases (2DEGs) with extremely high mobility. In the presence of an intense magnetic field, the suppression of scattering events that destroy the electronic phase coherence enables the formation of highly degenerate quantum states, called *Landau levels* (LL).

The interest in the development of solid state quantum devices goes well beyond fundamental research on many-body systems. The most amazing (and disconcerting) issue in quantum mechanics is the entanglement of identical particles. In the last decade entanglement has become synonymous with *quantum computing*. So far, a number of physical systems were proposed as possible candidates for quantum computing hardware [1] and many groups are working in this field to explore these options and to identify the best solution for practical devices.

In this context, the peculiar properties of QH systems can be very useful. First of all, being implemented in solid state devices, they can be easily miniaturized and integrated on chip by means of well-established semiconductor-technology fabrication methods. More fundamentally, QH circuits operate with electrons: due to their fermionic statistics, it is much easier to obtain a single-electron than a single-photon source. Moreover, in QH systems, the Lorentz force compels electrons to move along counter-propagating chiral channels at sample edges. When the LLs in the bulk are fully occupied, backscattering between counter-propagating edge states is drastically suppressed. When several LLs are populated, edge channels consist of a series of dissipationless edge states, that can be easily separated and indipendently contacted much like a computer bus. Edge channels in the fractional QH regime are even more interesting, since their excitations are

expected to display *anyonic* statistics [2]. Transport experiments [3, 4] suggested a further puzzle: due to electron-electron interactions, an individual integer edge channel seems to have a non-trivial inner structure: depending on the local density at the edge, the electron phase can be compressible or incompressible, giving rise to a series of isolated stripes that can be separately contacted.

A two-particle entangler can in principle be obtained by subsequently mixing counter-propagating and co-propagating edge channels [5]. While coherent mixing between counter-propagating edge states was achieved by means of quantum point contacts [6], a coherent mixer operating between co-propagating states has not been demonstrated yet. Samuelsson *et al.* proposed a solution to avoid the need to mix edge channels from different LLs [7]. These authors proposed an electronic analogue of the Hanbury–Brown–Twiss interferometer, which was demonstrated experimentally in 2007 [8]. Such devices have nevertheless several drawbacks caused by their non-simply connected topology. Besides the practical difficulty to contact microscopic isolated ohmic contacts, it is not obvious how to concatenate many devices in series, i.e. how to achieve *scalability*. On the contrary, Giovannetti *et al.* [9] recently theoretically showed that if a coherent mixer between co-propagating edges is indeed realized, scalable simply-connected interferometers can be build. Such devices could in principle work with *many* modes, if implemented in QH systems with filling factor $\nu > 2$. This advantage, along with the scalability, could be pivotal to unfold the potential of quantum circuits as electron entanglers and open the way to an innovative class of quantum computing devices.

The application of this scheme to the quantum computation of anyonic qubits crucially depends on the ability to determine (i) how parallel edge channels can be mixed, and whether this mixing is coherent or not; and (ii) the inner structure of edges, and in particular to determine possible fractional components that could be used as a bus of anyonic quasi-particles. The present thesis is aimed at experimentally addressing these challenging questions. To this end, we exploited a scanning probe microscopy (SPM) technique to directly manipulate edge channels. With the term "manipulate" here we mean indeed to pull, push, squeeze, displace quantum states by means of the electrostatic potential induced by a metallic tip, which acts as a scanning gate.

The first goal of our work has been to exploit the *scanning gate microscopy* (SGM) technique to extract spatially-resolved information about the edge-channel inner structure. As will be shown in chapter 3, our SGM maps provide the first images of the fractional stripes that form the inner-edge structure. The high resolution of the SGM technique allowed us to directly measure stripe widths and compare them with the predictions of the edge electrostatics theory [10]. Next, we designed a QH circuit whose geometry can be controlled at low temperature by moving the tip. Such an

innovative device was employed to locally investigate the microscopic processes that are responsible for the charge equilibration of bias imbalanced co-propagating channels. We will discuss how such device can be exploited as a beam mixer in simply-connected Mach-Zehnder interferometers.

This thesis is structured as follows:

- **Chapter 1.** A brief introduction to the physics of QH circuits is presented. This part is aimed at introducing all the fundamental physical issues we deal with in the following chapters.
- **Chapter 2.** We review and discuss the most relevant SPM techniques applied to the study of QH systems.
- **Chapter 3.** We report the results of our SGM experiments on quantum point contacts in the QH regime. We show the first images of the alternating fractional compressible and incompressible stripes, which form the inner structure of integer edge channels.
- **Chapter 4.** We demostrate a size-tunable QH circuit, and we show how the SGM can be exploited to image the scattering processes between co-propagating edge channels.
- **Chapter 5.** We summarize the main results of this thesis, and discuss future perspectives and developments.

Chapter 1

Transport in quantum Hall systems

In the solid state it is not easy to generate a self-focused one-dimensional (1D) beam of electrons that can propagate along the desired trajectory without dissipation or backscattering. It is even harder to achieve a long coherence length, to locally probe the chemical potential, to generate terahertz radiation, or to coherently split the electron wave in two paths. All these features are naturally built-in in quantum Hall (QH) systems. As a consequence they were successfully used to implement coherent circuits as, for instance, quantum electron interferometers.

Since QH systems play a central role in this work, in this chapter we shall review some of the most relevant aspects of the edge channel physics in both the integer and the fractional QH regimes.

1.1 The integer quantum Hall effect

The typical device used to observe the QH effect is schematically depicted in Fig. 1.1(a). It is called *Hall bar* and consists of a rectangular 2DEG with a source and a drain contact that allow to drive current along one axis of the sample, and pairs of contacts used to probe the voltage either on the same or on opposite sides of the bar. The classical theory predicts that the Hall resistance $R_H \equiv R_{xy} \equiv V_{xy}/I_0$ is proportional to the perpendicular magnetic field B, while the longitudinal resistance $R_{xx} \equiv V_{xx}/I_0$ is a constant which depends on mobility. However, if we perform the measurements on a high electron mobility sample at low temperature, we can observe a departure from the classical behavior in correspondence to peculiar values of the magnetic field. For such values R_H and R_{xx} display plateaus and minima, respectively. Figure 1.1(b) shows the results of a four-wire measurement of both the longitudinal and the Hall resistance, as a function of the magnetic field. We performed this measurement (called Shubnikov-de Haas measure-

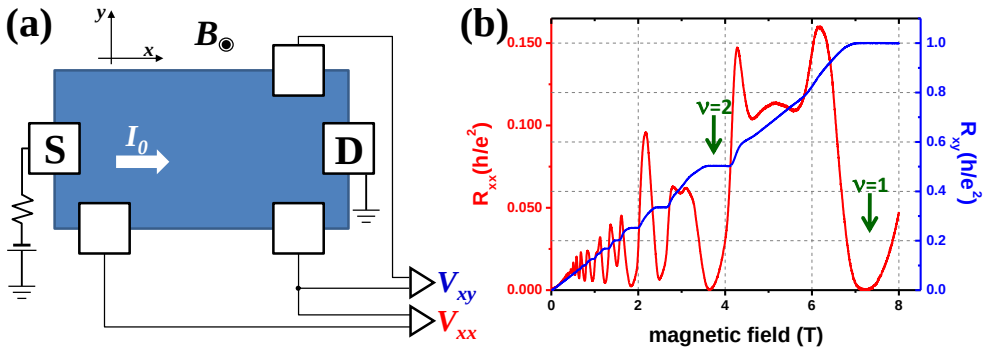

Figure 1.1: (a) Sketch of the typical setup used to measure the QH effect. While a bias current I_0 is driven between the source (S) and drain (D) contact, two pairs of voltage probes allow to detect the voltage drop across the Hall bar (V_{xy}) and along one edge (V_{xx}). (b) Longitudinal (R_{xx}) and Hall (R_{xy}) resistance measured on sample **A**, at 400 mK.

ment) at 400 mK on sample **A**,[1] whose mobility and sheet electron density are $\mu_A = 4.6 \times 10^6$ cm^2/Vs, and $n_A = 1.77{\times}10^{11}$ cm^{-2}, respectively.

The integer QH effect can be explained on the basis of the quantized 2D motion of independent electrons in a high magnetic field, in the presence of a confining potential and a small amount of disorder. The magnetic field quenches the electron kinetic energy in a discrete set of quantum levels, called Landau levels (LLs), whose energy spacing is given by the cyclotron energy $\hbar\omega_c \equiv \hbar eB/m^*$. The degeneracy per unit area of such levels is

$$n_L = \frac{eB}{h} \equiv \frac{1}{2\pi\ell_B^2}, \tag{1.1}$$

where ℓ_B (the so-called *magnetic length*) is the fundamental length scale for QH phenomena. The number of occupied LLs is expressed by the filling factor, defined as the ratio between the total electron density of the 2DEG n_0 and the LL degeneracy:

$$\nu \equiv \frac{n_0}{n_L} = \frac{n_0 h}{eB}. \tag{1.2}$$

By sweeping the magnetic field, we can change the number of occupied LLs, and thus the chemical potential of the 2DEG. Plateaus in R_H and minima in R_{xx} occur when ν is an integer number, i.e. when LLs are either fully occupied or empty. If the electron temperature is smaller than the LL energy spacing, no low-lying excitations are present. Therefore the 2DEG bulk is *gapped* and behaves as an insulator. In these conditions, charge is

[1] All samples reported in this thesis are listed in Appendix C.1, together with their main parameters.

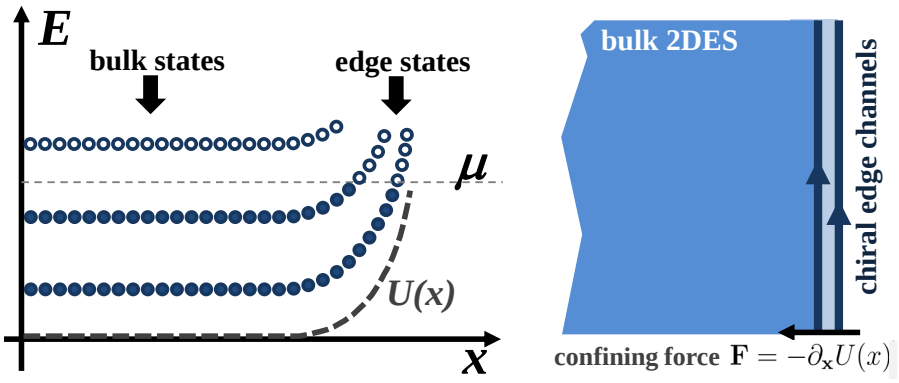

Figure 1.2: By tuning the magnetic field it is possible to set the chemical potential between two consecutive LLs in the bulk. In this case the filling factor is integer ($\nu = 2$ in this sketch) and the bulk behaves as an insulator. Gapless excitations can only occur at the sample edge, where the confining potential $U(x)$ bends the LLs upward. As in the classical case, the group velocity of the electrons is directed along $\nabla U \times \mathbf{B}$. This vector changes sign at the opposite sides of the QH liquid, so that charged excitations give rise to *chiral* 1D channels.

only carried by chiral 1D channels at the sample edge. The edge-channel picture is due to Halperin [11], and is based on the observation that an external potential is necessary to confine electrons in a sample of finite size. If this potential is sufficiently smooth, it can be treated as a perturbation that gradually increases the LL energy at the edge. Therefore, low-energy excitations can occur at the intersection between the chemical potential and the perturbed LLs, as shown in Fig. 1.2. The group velocity of these excitations has opposite sign at opposite edges, i.e. the QH system is *chiral*. The propagation direction is the same as that of the classical skipping orbit describing the motion of an electron subject to a vertical magnetic field and a horizontal electric field. The large (compared to ℓ_B) spatial separation between counter-propagating edge states prevents electron backscattering. This picture makes it possible to explain the curves in Fig. 1.1(b). When we apply a non-zero voltage V_0 between source and drain contacts, we imbalance the electrochemical potential between the upper (right-moving) and the lower (left-moving) edge channels, since, owing to chirality, they are in equilibrium with the source and the drain contact, respectively. The excess of right-moving electrons yields a net source-drain current (see Appendix A)

$$I_0 = \frac{\nu e^2}{h} V_0. \tag{1.3}$$

When the bulk is gapped, backscattering is suppressed and the electrochemical potential is constant along each edge. Therefore the voltage difference

between two points on the same side of the Hall bar is zero, while it is V_0 between points sitting on opposite edges. As a consequence, we measure $R_H = h/\nu e^2$ and $R_{xx} = 0$.

One final element is needed to explain the curves in Fig. 1.1: disorder. In fact, in a perfect system the number of edge states (which scales as the sample length) is negligible with respect to the number of bulk states (which scales as the sample area), so that the bulk would be gapped only for exact, discrete values of the magnetic field B, i.e. $B = n_0 h/\nu e$. The *finite* width of plateaus for R_H and zeroes for R_{xx} can be explained by considering that when a LL is populated, the first occupied states are localized around the local minima of the disorder potential. These localized states do not contribute to transport, while they do contribute to the density of states between LLs. The transport characteristics cannot change until all the localized states are occupied, so that R_H and R_{xx} are found to be constant for a finite range of B values.

In the description presented so far, we completely neglected the spin degree of freedom. To first order, it can be taken into account by adding the Zeeman term $\pm g^* \mu_B B/2$ (where g^* is the effective Landé factor) to the single–particle Hamiltonian. Both the Zeeman and the cyclotron energy depend linearly on magnetic field, though the former is about 70 times smaller than the latter due to the effective values of the electron mass and Landé factor in AlGaAs/GaAs structures. Exchange interactions can, however, significantly affect the actual Zeeman gap [12]. This is not the only effect of electron-electron interactions. In the next sections we shall discuss their dramatic impact on a highly degenerate ground state as a partially filled LL, and their role in determining the screening properties of the 2DEG.

1.2 The fractional quantum Hall effect

What happens if we increase the magnetic field beyond the $\nu = 1$ point in the plot of Fig. 1.1(b)? From the non-interacting model presented so far, we do not expect anything of interest. The degeneracy of the first LL is now higher than the total number of electrons, and the many-body ground state should be strongly degenerate. Figure 1.3 shows the results of the Shubnikov-de Haas measurement reported in Ref. [13]. Notably, plateaus and minima are also observed for peculiar fractional values of the filling factor. The discussion in the previous section indicates that for such values the 2DEG is gapped. This behavior was discovered in 1983 by H. L. Störmer and D. C. Tsui [14], and is called *fractional QH effect*. It can only be explained by taking electron correlations into account. The first theoretical model of the fractional QH effect was provided by R. B. Laughlin [15], who found that for $\nu = 1/(2p+1)$ (where p is an integer number), there exists a particular arrangement of the electrons that reduces the total energy. Such

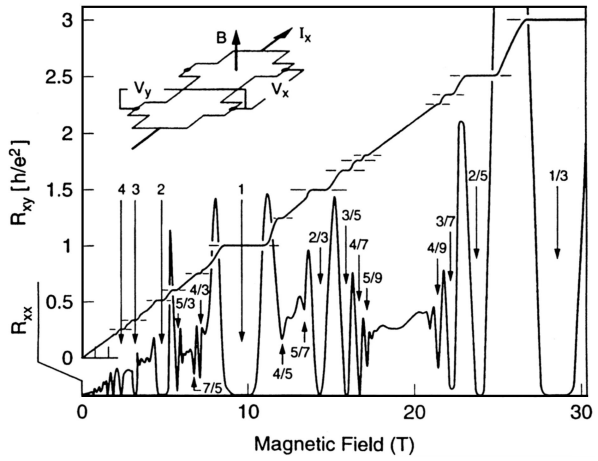

Figure 1.3: Plot of the Shubnikov-de Haas measurement reported in Ref. [13]. The minima in R_{xx} and the plateaus in R_{xy} observed for $\nu < 1$ ($B > 10$ T) cannot be explained by a single-particle model. The fractional QH effect is a many-body phenomenon.

arrangement is described by the *analytical* many-body wavefunction [15]

$$\Psi^L_{2p+1}(z_1, ..., z_N) = A \prod_{i<j} (z_i - z_j)^{2p+1} \prod_k e^{-|z_k|^2/4\ell_B^2}, \tag{1.4}$$

where $z_k \equiv (x_k + iy_k)/\ell_B$ is a complex variable representing the position (x_k, y_k) of the k-th electron in the 2DEG and A is a normalization constant. The polynomial part takes into account both the antisymmetry with respect to the permutation of any two electrons and electron-electron repulsion, since each electron sees an m-fold zero at the position of the other electrons. This wavefunction is exact for systems with few electrons (from 3 to 10), as confirmed by numerical simulations. Laughlin demonstrated that the ground state described by Eq. 1.4 is incompressible, i.e. perturbations smaller that a finite excitation gap cannot change the density. This excitation gap is of the order of one tenth of $e^2/\varepsilon\ell_B$, which corresponds approximately to the energy required to add a disk with area h/eB and charge νe to the 2DEG [16]. For larger perturbations the electron system nucleates localized regions with higher density. Such charge-density excitations display rather interesting features. They can be described as quasi-particles carrying fractional charge $q^* = \nu e$, and can be experimentally revealed by measuring the shot-noise signal in tunneling experiments [17].

The wavefunction in Eq. 1.4 describes the so-called Laughlin series, i.e. the fundamental sequence of filling factors $\nu = 1/(2p+1)$. This sequence can be extended by considering that excitations of a Laughlin ground state can rearrange themselves to generate a daughter ground state [18]. It is possible to iterate this procedure to generate the following hierarchy of filling

factors:

$$\nu = \frac{q}{2qp \pm 1}, \tag{1.5}$$

where both q and p are positive integers numbers. The series in Eq. 1.5 cover almost all filling factors experimentally observed. However, the hierarchy of the ground states does not correspond to the actual relative amplitude of the excitation gaps. For instance, the existence of fractions such as 6/13, that belong to the fifth generation, is well established experimentally.

An alternative approach to the description of fractional QH systems is provided by the theory of composite fermions, developed by J. K. Jain [19, 20]. The idea of this method is to replace the electron-electron interaction term in the many-body Hamiltonian by a fictitious vector potential acting on the electrons. Then, the mean value of this field is taken, so that the resulting Hamiltonian is actually single-particle and can be solved in the same way as for the integer QH effect. The change in the many-body Hamiltonian is equivalent to the attachment of $2p$ quanta of magnetic flux to each electron. Such flux quanta are directed in the opposite direction with respect to the external field. Each bound state of one electron and $2p$ flux quanta is called *composite fermion*. It moves in the mean field generated by all the other composite fermions plus the external magnetic field. The effective magnetic field experienced by the composite fermions is thus

$$B^* = B - 2p\frac{h}{e}n = B(1 - 2p\nu). \tag{1.6}$$

In Jain's theory the fractional QH effect is thus the integer QH effect for composite fermions. The actual filling factor (ν) is deduced from the effective integer one (ν^*) via Eq. 1.6:

$$\nu = \frac{\nu^*}{2p\nu^* \pm 1}. \tag{1.7}$$

Equation 1.7 provides the principal sequences of filling factors at which fractional QH states are experimentally observed.

We pointed out that a change in the electron density of both integer and fractional QH liquids costs a finite amount of energy, i.e. these systems behave as incompressible liquids. *Finite* incompressible liquids, however, can support gapless excitations at the edge [11]. These excitations consist in modulation of the boundary shape that preserve the total area. The edge can be described as the boundary between two regions with electron density $n = \nu eB/h$ and $n = 0$, respectively, in presence of a magnetic field ($\mathbf{B}$) orthogonal to the 2DEG plane and an in-plane confining electric field ($\mathbf{E}$) orthogonal to the edge. By the Lorentz force a density wave propagates along the edge with velocity $\mathbf{v} = (\mathbf{E} \times \mathbf{B})/B^2$. In 1990, Wen showed [21, 22] that fractional edge states behave as *chiral Luttinger liquids*. Due to their peculiar phase space, interactions in one-dimensional electron

systems (1DES) cannot be treated perturbatively. Interactions dramatically impact the ground state occupation of the electron liquid, which displays a non-fermionic behavior. Before the discovery of the QH effect, Luttinger liquids had only been studied theoretically [23] because of the difficulties encountered in the fabrication of clean 1DES. Fractional edge states provide a valuable tool to experimentally test the predictions of the Luttinger liquid theory, for instance by studying the zero-bias charge transfer between two counter-propagating edge channels brought into close proximity [24–27].

1.3 The reconstruction picture

The occurrence of a finite gap for bulk excitations in a partially filled LL is not the only effect of electron-electron interactions. These also impact the ability of the 2DEG to screen external potentials. In a gapped system screening is suppressed owing to the Pauli principle. Electron density is constant in the bulk and displays jumps of n_L in correspondence to each edge channel, as shown in Fig. 1.4(a). In any realistic sample such jumps actually have finite width. This implies the occurrence of a compressible region where the screening of the confinement potential is highly effective. In order to quantitatively and self-consistently determine the actual density profile and the extent of the compressible and incompressible regions, Chklovskii *et al.* [10] took electron-electron interactions into account in the mean-field approximation. The first step of their work consisted in classically calculating the electron-density distribution for a given confining potential in the absence of a magnetic field. In their analysis, the authors considered only a smooth confining potential defined by applying a negative voltage V_g to a metal gate fabricated on the sample surface. Due to the smallness of the $\hbar\omega_c/eV_g$ parameter, the electron density profile is not significantly altered by the magnetic field. In fact, any variation would require a large amount of work against the electrostatic forces. The only effect of the magnetic field is to change the screening radius as a function of the local filling factor

$$r_s = \begin{cases} \infty & \text{if } \nu = k \\ 0 & \text{if } \nu \neq k, \end{cases} \tag{1.8}$$

where k is an integer number. Let us consider the case of a bulk filling factor $1 < \nu_b < 2$. In this case a single incompressible region is expected to occur at the positions x_1, where $\nu(x_1) = 1$. This incompressible stripe (IS) has a finite width because the system can gain energy by relocating electrons from the second LL to the first one in the vicinity of x_1. In general, the width of the k-th incompressible region can be calculated by assuming that the drop of the external potential at its edges is $\Delta\mu_k/e$, where $\Delta\mu_k$ is the chemical potential jump between the k-th and the $(k+1)$-th LL. The estimate found

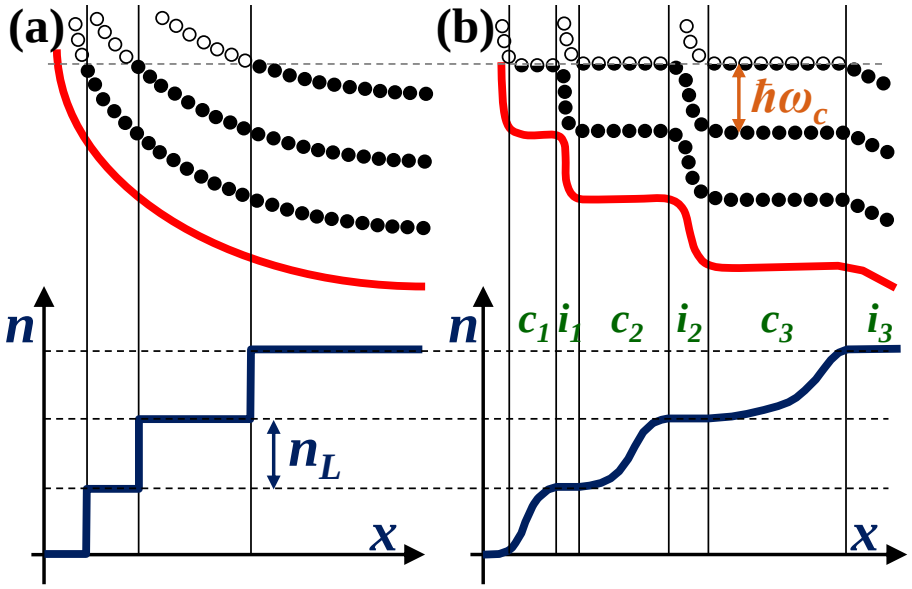

Figure 1.4: (a) The single-particle model for the edge of a QH system. The confinement potential (red line) can be considered as a perturbation of the single-particle energies. A finite jump in the electron density $n(x)$ occurs whenever a LL crosses the chemical potential. (b) In the reconstruction model the confinement potential is screened when the electron density is *not* a multiple of n_L. Such regions (c_i) are compressible, thus the electron density can vary. On the other hand, when $n = kn_L$, the electron phase is incompressible and the screening is suppressed. The width of the incompressible stripes depends on both the gap between the LLs and the local gradient of the electron density.

by Chklovskii *et al.* for such a width is given by [10]

$$a_k^2 = \frac{4\Delta\mu_k\varepsilon}{\pi^2 e^2 dn/dx|_{x=x_k}}. \tag{1.9}$$

For spin-degenerate integer edge channels, where $\Delta\mu_k = \hbar\omega_c$, it becomes:

$$a_k^2 = \frac{1}{2}\frac{4\hbar\omega_c\varepsilon}{\pi^2 e^2 dn/dx|_{x=x_k}}, \tag{1.10}$$

where the factor 1/2 incorporates spin degeneracy. Figure 1.4(b) helps the comparison of the model by Chklovskii *et al.* (called *reconstruction picture*) with the non-interacting model. In the reconstruction picture, the edge channel is seen as a series of alternating compressible and incompressible stripes. Within the compressible stripes (CSs) the external electric field is perfectly screened and the density smoothly varies, while inside the incompressible region the electron density is constant and the external potential sharply varies.

It must be stressed that the fundamental ingredient of the reconstruction picture is the dependence of screening on the local compressibility. Therefore, we expect that when the density equals a Jain's fraction, the screening will be suppressed as well. As a consequence Eq. 1.9 can be generalized to any (fractional or integer) gap [10]:

$$a_f^2 = \frac{4\Delta\mu_f\varepsilon}{\pi^2 e^2 dn/dx|_{x=x_f}}, \tag{1.11}$$

where a_f is the fractional incompressible stripe width, and $\Delta\mu_f$ is the gap in the chemical potential corresponding to the fractional incompressible phase. This implies that even the edge of a simple $\nu = 1$ QH system has a non-trivial structure determined by the fractional incompressible stripes. A signature of such an inner structure was experimentally found by Kouwenhoven *et al.* [3], and discussed theoretically by Beenakker [28] even before the quantitative analysis of Ref. [10]. In their experiment Kouwenhoven *et al.* showed that is possible to selectively populate the different fractional components of a "nominally" single integer edge channel. The occurrence of an edge reconstruction was suggested also by other experiments [4, 29]. However, a direct measurement of the spatial details of the inner edge structure has only become possible recently, and exclusively for integer incompressible stripes, while information about the fractional components is still missing. Experimental investigations of the spatial details of the edge channels are based on innovative scanning probe microscopy (SPM) techniques, which will be discussed in chapter 2.

1.4 Quantum Hall interferometry

The chirality and the absence of backscattering make QH edge channels the ideal building block for coherent quantum circuits. Examples are the implementation of electron interferometers in Mach-Zehnder [6, 30–32], Fabry-Pérot [33], and Hanbury-Brown-Twiss [8] configuration. In these fascinating devices the electron "beam" runs along the confinement potential, which can be suitably designed by means of Schottky gates fabricated on top of the heterostructure. Beam-splitters are obtained by defining constrictions in the 2DEG (the so-called quantum point contacts, QPCs) that allow to coherently induce backscattering by reducing the separation between counter-propagating edge states. QPCs can be realized by negatively biasing two split-gates in order to deplete the 2DEG underneath. The constriction is thus defined by the "electrical" gap between the gates. Finally, ohmic contacts are used to inject and remove electrons.

Soon after its demonstration, the Mach-Zehnder interferometer (MZI) attracted a considerable interest, due to its possible applications to the study of dephasing and decoherence [34], to the observation of fractional statistics

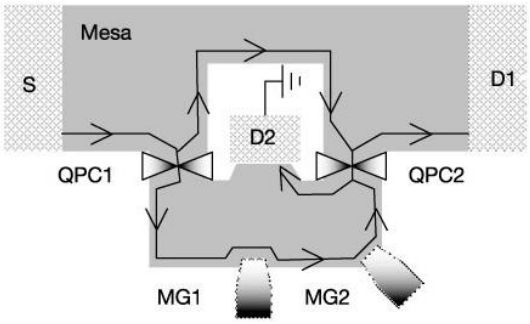

Figure 1.5: Sketch of the first electronic Mach-Zehnder interferometer. From Ref. [6].

of quasi-particles [35, 36] and to the demonstration of their interference [37]. The scheme of an electronic MZI is shown in Fig. 1.5. Electrons are injected from the source contact **S** on the left. They propagate along the sample edge until they reach **QPC 1**. The bias applied on this QPC is tuned so that the induced backscattering probability is exactly 50%. The incoming edge current is then split into two paths, a transmitted inner path and a reflected outer path. The two coherent components of the electron wavefunction recombine and interfere at **QPC 2**. As a result, the two current signals detected on contacts **D1** and **D2** oscillate out of phase as a function of the relative Aharonov-Bohm phase between the two paths. Since there is no electron loss, the sum of the two signals is constant and equals the total current injected by the source. The Aharonov-Bohm phase φ is given by $\varphi = 2\pi BA/\Phi_0$, where B is the magnetic field, A is the area enclosed by the two paths, and $\Phi_0 = 4.14 \times 10^{-15}$ Wb is the quantum of magnetic flux. Therefore, in order to sweep φ one can vary either A or B. A simple way to control A consists in applying a negative bias to a modulation gate **MG** in order to gradually deplete a small portion of the area A. In most experiments the control of B is obtained by short-circuiting the superconducting coil that generates the magnetic field. In this kind of superconductors the persistent current is not strictly constant, but smoothly decays with a rate of about 0.1 mT/h.

The constantly growing flexibility in the practical implementation of QH circuits stimulates further investigations and different designs, in order to overcome the intrinsic limitations of the standard MZI architecture. Such limitations are both practical and fundamental, and are ultimately related to the MZI topology. From the practical point of view, this design requires an air-bridge to contact the **D2** detector and the inner QPC gates, which makes the fabrication process more difficult. From a fundamental point of view, the area A enclosing the two paths must include the etched region containing the **D2** contact. Therefore A cannot be made smaller than several tens of

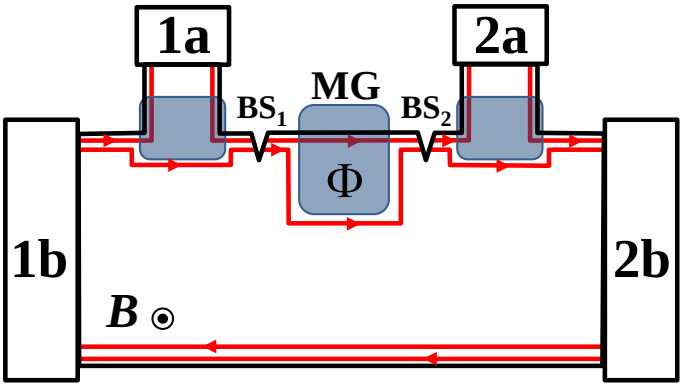

Figure 1.6: Scheme of the simply-connected MZI proposed by Giovannetti *et al.* in Ref. [9].

square microns, so that a small perturbation in the magnetic field induces a large fluctuation of the total flux. This can result in a difficult control of the total flux. Moreover, with this geometry it is difficult to concatenate more than two devices in series, a possibility that would open the way to the implementation of a number of scalable devices, and quantum information architectures.

An alternative, simply connected, MZI architecture was proposed by Giovannetti *et al.* [9]. Figure 1.6 shows this design, which is based on the idea that to avoid a topological hole in the 2DEG it is necessary to coherently mix two *co-propagating* (i.e. on the same sample edge) edge channels. The two components, both propagating from source contact **1b**, can be separated by means of negatively biased Schottky gates that send one of them to an ohmic contact (**1a** in the scheme) at a different chemical potential. Thus, when the two edge channels are put again in interaction, they have an electrochemical imbalance, whose amplitude is controlled by the applied signal. The beam splitter $\mathbf{BS}_1$ allows electrons to select between two distinct paths, which are then separated by the modulation gate **MG** so that they acquire a relative phase Φ. Carriers are mixed again in $\mathbf{BS}_2$ and then sent to two contacts **2a** and **2b**.

Except for the beam splitters, all the components of this device are relatively standard elements for nanofabrication technology. The scattering mechanisms that allow to coherently transfer electrons between co-propagating channels are not known in detail. To date, experiments studying the transport between co-propagating channels could only provide information on the cumulative effect of the processes taking place along the whole beam splitter length. The need of a spatially resolved investigation motivated us to apply scanning probe techniques to reveal the source of inter-channel scattering. These experiments will be described in chapter 4.

Chapter 2

Scanning probe microscopy and quantum Hall systems

Progress in nanoscience owes much to the advances in SPM techniques. The crucial role of the scanning probe technology is witnessed by the Nobel prize assigned in 1986 to Gerd Binnig and Heinrich Rohrer for the design of the scanning tunneling microscope (STM). Scanning probe techniques are a powerful interface to the nanoworld: they allow us to "see" and "manipulate" nanostructures, down to the atomic scale. Modern nanoscopy does not merely target sample imaging, but allows to experimentally probe a broad range of physical characteristics, e.g. electronic density of states, electromagnetic near-field profiles, local electrostatic potentials, surface stiffness and viscosity, local work function, etc. The ability to probe electronic properties at the nanoscale vastly impacted the investigation of mesoscopic systems. SPM techniques can directly access and *image* quantum phenomena (impressive examples are given in Figs. 2.4 and 3.2). The implementation of SPM setups operating in cryogenic conditions opened the way to their exploitation to study the QH regime. First SPM developements in this field aimed at measuring the local electric potential and charge density. The measurement of such quantities on QH systems made it possible to image and study localized states in the bulk, the Hall potential distribution, the electrochemical potential, and the compressibility profile at the sample edge. This motivated us to combine the experience gained by our quantum transport group with the opportunities provided by SPM.

In this chapter we discuss advantages and limitations of existing SPM setups. In particular, in the first section we review the main SPM techniques applied to the investigation of QH systems, i.e. the single electron transistor scanning electrometer, the Kelvin probe force microscope, and the scanning capacitance microscope. Such techniques (developed in the late 90s) allow to locally measure the Hall potential and electron compressibility, and therefore to image edge channels. In the second section, we shall introduce the

pioneering experiments of scanning gate microscopy (SGM), the technique exploited for our experiments in the QH regime.

2.1 Imaging quantum Hall systems by scanning probe microscopy techniques

Single electron transistor scanning electrometer (SETSE)

The *single electron transistor scanning electrometer* (SETSE) employs the most advanced probe among SPM techniques. It consists of a specially shaped glass fiber with a single electron transistor (SET) located at its tip [38, 39]. The SET is obtained by fabricating two metal leads (source and drain) onto the glass tip, as sketched in Fig. 2.1(a). The leads are connected to a small (100 nm) island by two tunnel junctions. The current I_{SET} tunneling through the junctions displays Coulomb blockade peaks as a function of the electrostatic potential experienced by the island from external sources. Since the peaks are sharp, the SET sensitivity is very high. Typical signal levels are of the order of $0.01e$ induced on the island. Maps of the surface potential V_{surf} are obtained by scanning the tip over the sample and simultaneously acquiring I_{SET}. The SETSE spatial resolution is of the order of the island size, i.e. ≈ 100 nm.

In the QH regime the high sensitivity of the SETSE (100 μV/Hz$^{1/2}$ [39]) was exploited to probe both localized states in the bulk [40, 41], and edge states at the sample boundary [39]. The latter can be identified by trans-

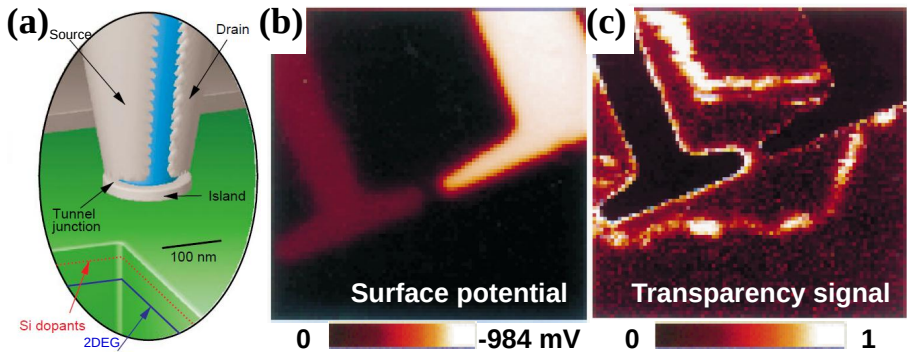

Figure 2.1: (a) Sketch of the SET probe suspended over a 2DEG. (b) Map of the electrostatic potential signal (V_{surf}) corresponding to a pinched-off QPC, in a 2DEG at $\nu_B > 2$. The gate biases are 0 V (left gate) and -0.6 V (right gate). (c) Map of the transparency signal $\delta V_{surf}/\delta V_{BG}$, where δV_{BG} is the applied back gate voltage modulation and δV_{surf} is the in-phase response measured by the SETSE. Transparent regions correspond to the incompressible stripes at $\nu = 2$ [39].

parency measurements, which are sensitive to the local compressibility. Such measurements require the presence of a back gate underneath the 2DEG. The compressibility is measured by modulating the back gate voltage V_{BG} by a small amount δV_{BG}. The surface voltage variation δV_{surf} measured by the SETSE depends on the local screening properties of the sample. The local compressibility κ can be extracted from the relation $\delta V_{surf}/\delta V_{BG} = C/e\kappa$, where C is the capacitance between the 2DEG and the back gate. Figure 2.1(c) shows the transparency map of a 2DEG constriction defined by two T-shaped gates, which can be recognized in the V_{surf} plot in Fig. 2.1(b). The transparency map reveals compressible and incompressible phases of the 2DEG, whose bulk filling factor is slightly higher than 2. The incompressible regions (high transparency signal) appear as stripes that meander across the image. As discussed in section 1.3 these structures are the fingerprint of edge reconstruction. The resolution of the SETSE maps allows one to image the edge trajectory, but is not sufficient to measure edge width or to reveal its inner structure, whose size is of the order of the magnetic length (≈ 15 nm).

Kelvin probe force microsopy (KPFM)

The local voltage of mesoscopic structures can also be measured mechanically, i.e. by an atomic force microscope (AFM) operating in non-contact mode. Figure 2.2(a) shows the typical setup for measurements in the QH regime: an AC potential V_0, oscillating with frequency ω_0, is applied to the source contact. It modulates the 2DEG electrochemical potential $\mu_{ac}(x,y) \equiv eV_{ac}(x,y)$, whose spatial distribution is to be measured. The local sample potential $V_{ac}(x,y)$ electrostatically interacts with the sharp, metallized AFM tip, deflecting the biased AFM cantilever with a force that can be modeled

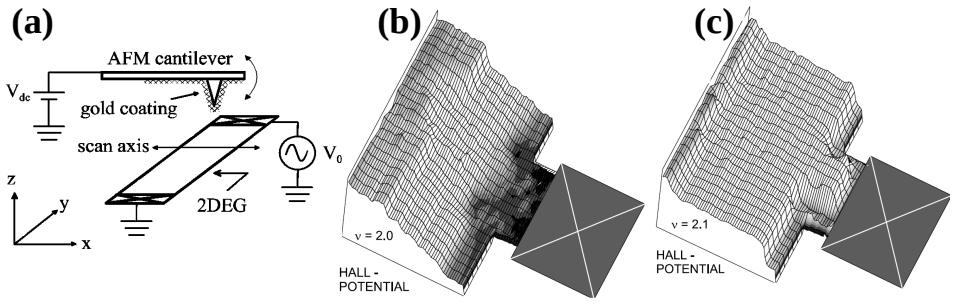

Figure 2.2: (a) Scheme of KPFM measurement [42]. (b) Hall potential distribution near a probe contact for bulk filling factor $\nu_b = 2$. The Hall potential drop is distributed along the whole sample width. (c) For filling factor $\nu_b = 2.1$ the Hall potential drops only at the sample edges, due to the effective screening of the compressible bulk [43].

as

$$F = \frac{1}{2}\frac{dC}{dz}[(V_{dc} - V_{CPD}) + V_{ac}(x,y)\sin(\omega_0 t)]^2, \tag{2.1}$$

where C is the tip sample capacitance, z is the tip sample separation, V_{dc} is the tip bias, and V_{CPD} is the contact potential between sample and tip. F has three components:

$$\begin{aligned} F_{DC} &= \frac{dC}{dz}[\frac{1}{2}(V_{dc} - V_{CPD})^2 + \frac{1}{4}V_{ac}^2(x,y)] \\ F_{\omega_0} &= \frac{dC}{dz}[V_{dc} - V_{CPD}]V_{ac}(x,y)\sin(\omega_0 t) \\ F_{2\omega_0} &= -\frac{1}{4}\frac{dC}{dz}V_{ac}^2(x,y)\cos(2\omega_0 t). \end{aligned} \tag{2.2}$$

The first and second harmonics F_{ω_0} allow one to determine $V_{ac}(x,y)$, the local electrostatic potential in the sample. This SPM technique is called *Kelvin probe force microscopy* (KPFM). It offers several advantages with respect to SETSE. First of all, it employs a much simpler and sharper probe, which ultimately yields sample *topography* with higher resolution. Moreover, one can obtain both $V_{CPD}(x,y)$ and $V_{ac}(x,y)$ maps. V_{CPD} is obtained by applying a feedback system on the tip bias in order to null the first harmonic (i.e. the term $(V_{dc} - V_{CPD})$), while V_{ac} is given by the second harmonic signal. Finally, the KPFM voltage sensitivity (10 μV/Hz$^{1/2}$ [42]) is about 10 times more accurate than in the SETSE [39, 42].

Panels (b) and (c) of Fig. 2.2 depict the experiment by Ahlswede *et al.* [43]. In this experiment the KPFM was used to image the Hall potential in the vicinity of an ohmic contact of a Hall bar. The measurement of the local Hall potential is a simple way (and an alternative to transparency measurements) to visualize edge channels. Due to their finite capacitance, an imbalance between counter-propagating edge channels produces a charge pile-up at the sample boundary that can be revealed by KPFM. Although the resolution of this technique (about 200 nm) is not sufficient to resolve individual incompressible stripes, it does visualize the effect of electron interactions.

Scanning capacitance microscopy

Scanning capacitance microscopy (SCM) is closely related to the KPFM technique. Indeed, the same setup can be used either for Kelvin probe or scanning capacitance measurements. SCM operation is schematically sketched in Fig. 2.3(a). A sharp conducting tip is positioned 5 nm above the sample surface and connected to a highly sensitive charge detector. An AC excitation voltage is applied to the 2DEG through an ohmic contact (2 mm away from the tip). No other contacts are made to the sample. The excitation causes charge to flow in and out of the 2DEG, which in turn

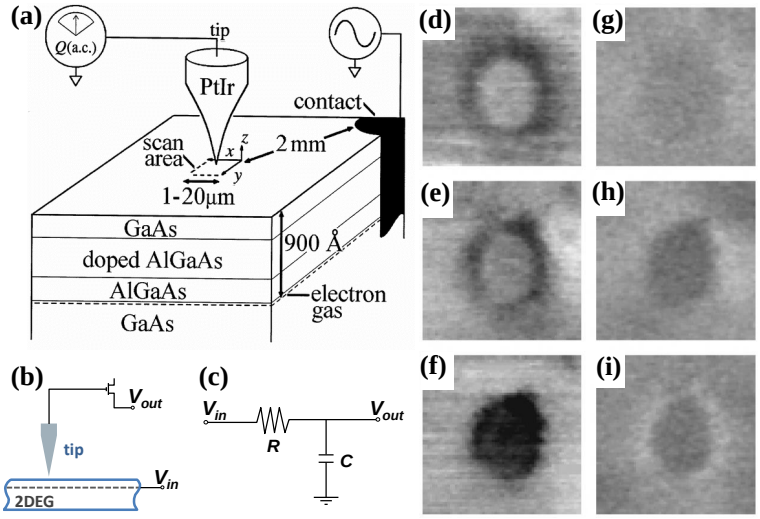

Figure 2.3: (a) Diagram of the SCM measurement configuration [44]. The SCM setup (b) can be represented by a RC circuit whose scheme is shown in (c). (d–f) 13 μm×13 μm SCM scans (in-phase signal) for (d) $B = 8.0$ T, (e) $B = 8.1$ T, and (f) $B = 8.2$ T. (g–i) Out-of-phase SCM signal for (g) $B = 8.0$ T, (h) $B = 8.1$ T, and (i) $B = 8.2$ T [45].

induces charge to flow in and out of the tip. By scanning the tip and using synchronous lock-in detection of the induced charge, one obtains a map of the charge accumulating in-phase (Q_{in}) with the excitation.

SCM allows to *directly* (i.e. with no need of a back gate) measure the local compressibility: in fact, when the tip is scanning an incompressible region, the SCM signal is zero, since these regions do not accumulate charge or conduct electricity. As a consequence SCM can probe reconstruction of integer edge channels. Figure 2.3(d–f) shows the results of SCM measurements on an intentionally induced charge perturbation[1] in a 2DEG with filling factor near $\nu = 2$. The three panels on the left show the in-phase signal with $B = 8.0$ T, 8.1 T, and 8.2 T ($\nu_b = 2$ for $B = 7$ T). Dark areas can be interpreted as 2DEG regions with reduced compressibility. They correspond to the incompressible stripe at $\nu = 2$ separating the bulk ($\nu_b < 2$) from the spot center ($\nu > 2$). In such regions the 2DEG below does not charge and discharge with the weak AC excitation. The lock-in technique allows to simultaneously acquire the out-of-phase SCM signal as well (Fig. 2.3(g–i)), which gives additional information about the conductivity of the 2DEG. In fact, the SCM setup can be approximately described as a RC circuit, as sketched in Fig. 2.3(b,c). Moving the scanning probe toward the regions in the interior of the incompressible stripe increases the effective resistance.

[1]The charge parturbation has been induced by holding the tip in a given position and applying approximately +3 V for 30 s.

This causes the measured in-phase signal to steadily decrease to zero, while the out-of-phase signal first increases from zero, reaches a maximum for $\omega = (RC)^{-1}$, and then decreases back to zero level.

SETSE, KPFM, and SCM allowed a first direct and spatially resolved analysis of integer incompressible stripes. They unambiguously demonstrate the modulation of the electron compressibility induced by interactions. The resolution of such methods, however, is not sufficient to obtain quantitative information about the size of the stripes. More "quantitative" measurements [46] became recently possible thanks to the significant leap in the resolution provided by the SGM technique.

2.2 Scanning gate microscopy

The SPM techniques discussed so far aimed at reducing as much as possible the influence of the tip, in order to probe to the best possible approximation the *unperturbed* electron system. The principle of operation of the SGM is in some sense opposite, since it uses a conductive AFM tip to intentionally perturb the electrons in order to measure the resulting effect on transport properties.

The development of SGM for the investigation of high mobility 2DEGs was pioneered by the Harvard group in the early 2000's [47, 48]. In their experiments they raster-scanned a negatively charged tip above a QPC and simultaneously measured the position-dependent conductance of the device. The negative tip bias creates a depletion spot in the 2DEG, which is used as a movable scattering center to reflect electrons flowing through the QPC. The split-gates of the QPC are biased in order to confine electrons in the transverse direction, and thus conductance plateaus for multiples of $2G_0$ are observed. This step is needed to focus the electrons, so that the tip can effectively scatter them back through the QPC. This effect is visualized by plotting the reduction of the trasmitted conductance as a function of tip position. The result is spectacular, as shown in Fig. 2.4. When the tip is scanned over regions with high current density, the conductance is significantly reduced, while in other regions it remains essentially unchanged. In this sense, SGM maps allow to visualize the actual electron flow.

The interpretation of SGM maps is different for scans near the QPC and for those far from it. In the former case, SGM scans correctly reproduce the electron wavefunction determined by the QPC potential. As shown in Fig. 2.4(b) [47], due to the confinement in the transverse direction, the wavefunction has a lobe structure. The number of lobes depends on the "effective" size of the constriction. In the absence of disorder, one would expect a regular broadening of the lobes in the regions far from the QPC center. On the contrary, the SGM maps reported in Fig. 2.4(c,d) reveal that the electron flow forks into several different paths, which continue to

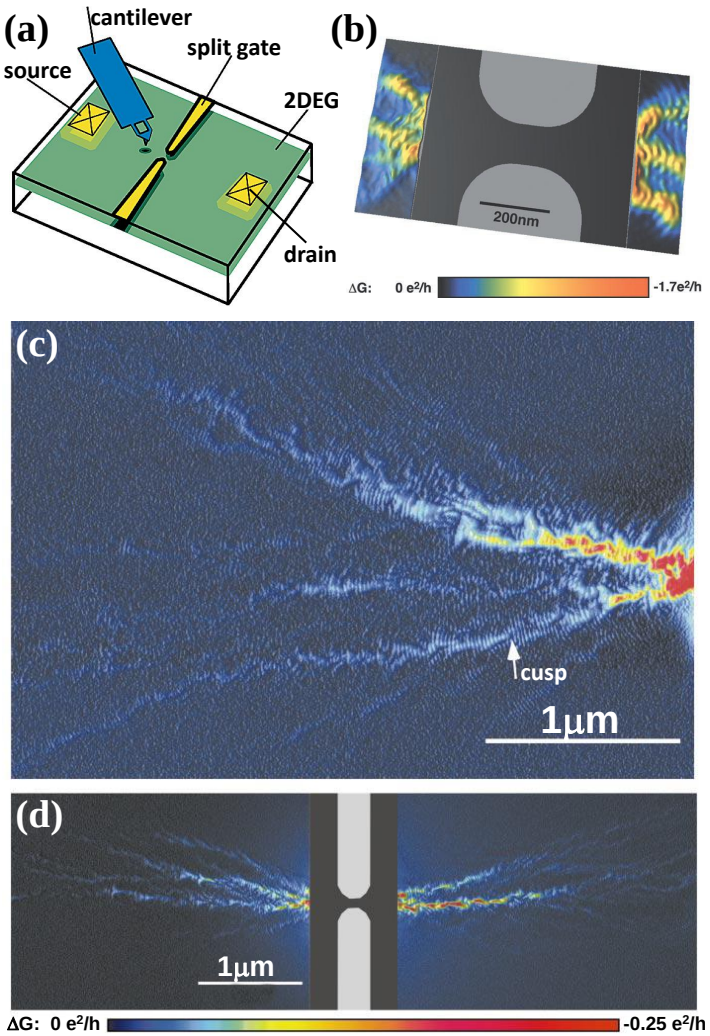

Figure 2.4: (a) Scheme of the SGM setup. The transmitted QPC conductance is measured as a function of the tip position [47]. (b) Map of the change ΔG in the transmitted conductance induced by the tip when scanned over the region near the QPC, which has been set to the third conductance plateau ($G = 6G_0$) [47]. (c) Image of the branched electron flow from one side of a QPC, biased on the first conductance step. Areas where the conductance is significantly changed by the the presence of the tip correspond to the regions of high electron flow. Due to the disorder potential, the electron trajectories form caustics, which are revealed as branches. In particular, a dip in the potential generates a cusp downstream, one of which is indicated by the arrow. The branches display clear fringes, whose spacing is $\lambda_F/2$. Such fringes are due to the intereference between indistinguishable events (electrons can be backscattered either directly into the QPC, or after being reflected from the split-gate potential) [48]. (d) Electron flow imaged from both sides of a different QPC [48].

branch off into ever smaller sub-branches for the full width of the scan. This peculiar branching phenomenon actually depends on the landscape of the disorder potential. The amplitude of most potential fluctuations is significantly smaller than the Fermi energy, so that the disorder perturbs the electron trajectories rather than directly backscatter them. In particular, potential valleys act like lenses that focus the electron paths, giving rise to cusps. One example of such a cusp is indicated by the arrow in Fig. 2.4(c). Due to the cumulative effect of all the small-angle scattering events induced by potential modulations, electron trajectories tend to accumulate and form *caustics*, which are revealed as branches [49].

The ability to backscatter electrons even for large (several microns) tip-QPC distances crucially depends on the fact that the motion is ballistic: electrons adiabatically follow time-reversed paths from the depletion spot to the QPC. In the diffusive regime the effect of the tip would be scarce and rather insensitive to position. The mean free path of electrons can thus be approximated as twice the length of the branches: in this example around 2 μm.

The presence of fringes decorating the branches reveals that the process is coherent. These patterns are interpreted as the result of the sum of quantum amplitudes for two indistinguishable events: electrons can be reflected directly back into the QPC, or backscattered by the split-gate potential, then again by the tip potential and finally reflected into the QPC.[2] By moving the tip for a distance of $\lambda_F/2$, the phase change for the former event increases by about $\delta\phi_1 = 2\pi$ (since the total path length increase is λ_F). For the latter event the phase change is $\delta\phi_2 = 4\pi$, so that the relative phase difference is $\delta\phi_2 - \delta\phi_1 = 2\pi$, i.e. the fringe periodicity is exactly $\lambda_F/2$.

[2]This effect is quickly suppressed as the number of reflections increases. Therefore, events with more reflections can be neglected to first approximation.

Chapter 3

Imaging edge-channel structure by scanning gate microscopy

Apart from the few examples discussed in chapter 2, the physics of QH edge channels was almost exclusively investigated by transport experiments. Despite the crucial role played by this kind of measurement in revealing the properties of these chiral 1D electron systems, very little information was obtained about the spatial features of the edge channels, and their inner structure. As discussed in the previous chapter, recently-developed low-temperature SPM techniques open the way to a deeper-than-ever investigation of spatial features of edge systems. Due to their resolution limits, however, these techniques could not reveal the inner structure of a *single* edge. As shown in section 1.3, the reconstruction picture predicts the occurrence of a series of compressible and incompressible stripes even within a single edge, due to the fractional QH effect. In this chapter we shall show how the SGM technique can be exploited to directly *image* both integer and fractional components of edge channels. The high spatial resolution provided by the SGM will allow us to quantitatively estimate, for the first time, the width of fractional incompressible stripes for the filling factors 1/3, 2/5, 3/5 and 2/3.

3.1 Experimental SGM setup

The SGM measurements shown in the present work were performed with an Attocube LT-SYS/He system. In this setup, the cryostat is inserted in a liquid helium (LHe) reservoir which is suspended by means of springs in a soundproof box, in order to damp vibrations induced by the lab floor and acoustical noise. The cryostat is a ^{3}He closed cycle refrigerator that can reach a base temperature of 300 mK at the cold finger. The dewar is

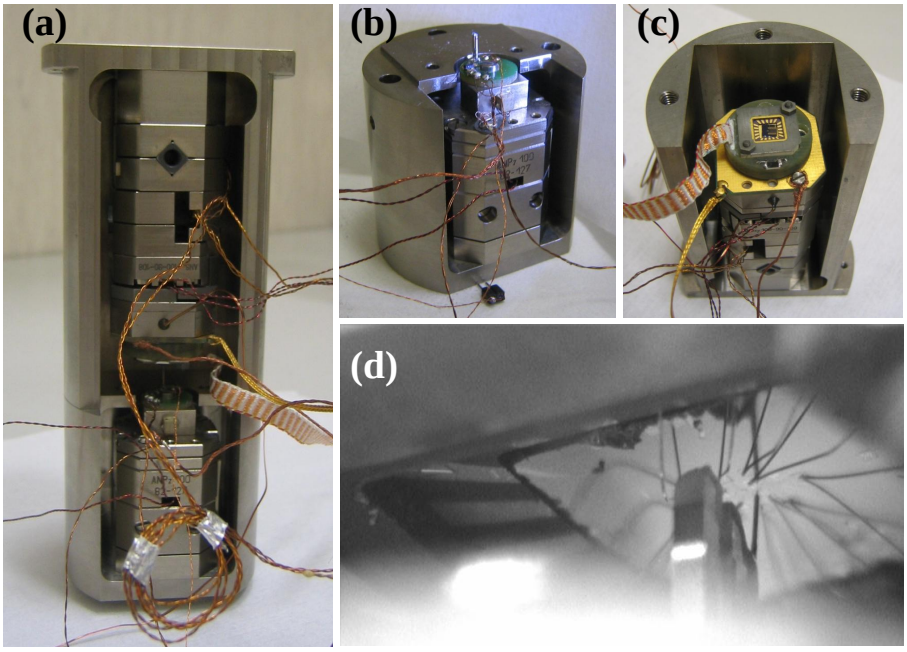

Figure 3.1: (a) AFM head. The stack of its modules is visible in both the top and the bottom part of the shell. These components can be better seen by dismounting the titanium body of the AFM. (b) The bottom part contains the Z coarse positioner and the tuning fork (TF) stage. (c) The top part contains the X and Y coarse positioners, the piezo scanner, the sample thermometer and the sample holder. (d) A CCD picture of the TF+tip system, acquired during a scan on a Hall bar.

equipped with a superconducting coil which provides magnetic fields up to 9 T. The AFM head (shown in Fig. 3.1(a)) is directly connected to the cold finger. The head is made by two stacks of elements mounted onto the half shells of a titanium body. The elements of the AFM are:

- *Coarse positioners:* three inertial actuators move the sample (X and Y positioners) and the tip (Z positioner) for long distances (5 mm) with a step precision of the order of 300 nm.

- *Scanner:* a piezoelectric ceramic actuator accurately moves the sample in all three directions.

- *Thermometers:* a RuO_2 resistive thermometer is placed just under the sample holder.

- *Sample holder:* a 20-wire chip-carrier holder connects the sample pins to the cryostat cables via *pogo-pin* connections.

- *Tuning fork (TF) system:* this element contains a metallic base with a dither piezo that excites mechanical vibrations, on which a printed circuit board is mounted with the TF together with the electronic components of the first amplification stage of the TF signal. The instrument is operated in *non-contact* tip-sample shear force mode. Sample topography is obtained by controlling the tip height in order to keep the TF oscillation amplitude constant.

Samples for SGM measurements are mounted on chip-carriers, such as the one shown in Fig. 3.1(c). In order to find the desired structure, we move the tip with respect to the sample by means of coarse positioners, using a CCD camera to visualize their relative position. The CCD camera allows to find the relevant sample structure with an error of the order of 50 μm. Then, we start the approach procedure, which is completed when the TF signal senses the surface. Subsequently, we locate the nanostructure under investigation using a coordinate pattern fabricated on the sample. AFM topography allows to locate the position of the scanned area, and thus to determine how many coarse steps in both X and Y direction are required to center the scan range on the desired device. Finally, we acquire the device topography to check its conditions, surface quality, and tip resolution. After these preliminary tests at room temperature, the tip is retracted approximately 500 μm away from the surface, and the sample chamber of the cryostat is evacuated and immersed in the LHe dewar for low temperature measurements. When the desired base temperature is reached, the tip is again approached to the sample. The cooling process typically induces an in-plane drift of the tip relative to the sample of the order of 50 μm, thus a further positioning step is needed. Again, the coordinate pattern is used to locate the device. For this reason, the coordinate spacing (5 μm) is chosen to be smaller than the low-temperature scan range (8.5 μm and 30 μm for the two scanners used).

3.2 Measurements at zero magnetic field

Though the goal of the present work is the spatially-resolved investigation of QH edge channels, our first experiments focused on a constriction in a high mobility 2DEG at zero magnetic field. There are two reasons for this choice. On one hand, as seen in section 2.2, constrictions in 2DEGs were investigated by Topinka *et al.* [47, 48]: we exploited their results as a reference to both validate our setup and characterize our samples. On the other hand, the same device provides a structure that allows to explore new physics by simply applying a high magnetic field, as we shall show in the next section.

As pointed out in chapter 1, the physics of the QH effect emerges in high mobility samples. All samples reported in this thesis were fabricated

starting from high mobility GaAs/$Al_{0.33}Ga_{0.66}As$ heterojunctions. For the experiments reported here we used two samples (labeled as **A** and **B**): sample **A** had a 2DEG buried 80 nm underneath the surface, with an electron sheet density $n_A = 1.77 \times 10^{11}$ cm^{-2} and a mobility $\mu_A = 4.6 \times 10^6$ cm^2/Vs. The 2DEG depth, the electron density and mobility for sample **B** were 80 nm, $n_B = 3.2 \times 10^{11}$ cm^{-2}, and $\mu_B = 2.3 \times 10^6$ cm^2/Vs, respectively. The device scheme for both samples is the same as the one shown in Fig. 2.4(a). A Hall bar structure with ohmic contacts was defined by UV lithography,[1] while split-gates with a gap of 300 nm were fabricated by electron beam lithography.

After locating the device as explained in the previous section, we acquired the topography of the split-gate center, which is the reference that allows to pinpoint the structures observed in the SGM maps. Then, another topography scan allowed us to determine the average surface plane, which is parallel to the 2DEG plane. Such preliminary scans were performed by keeping both gates and the tip grounded, in order to avoid a short that could potentially destroy the split-gates. Then, the tip was lifted 10 nm above the surface and biased to $V_{tip} = -5$ V. Split-gates were biased in order to set the QPC to a conductance plateau (so that the transmitted conductance G_T is a multiple of $2G_0$). SGM conductance maps were obtained with the negatively biased AFM tip scanning two regions on either the left or the right side of the QPC, while simultaneously measuring the transmitted source-drain current. This was done using a current preamplifier in a two-probe configuration. Contact resistances were subtracted numerically. The SGM map in Fig. 3.2(a) was taken with the QPC of sample **B** set to the third conductance plateau ($G_T = 6G_0$). It shows the change in conductance $\Delta G = (I_{SD}/V_{SD}) - 6G_0$ (where V_{SD} and I_{SD} are the source-drain bias and current, respectively) as a function of the tip position in the two scanned areas. Figure 3.2(b) shows an analogous SGM scan on the left side of the QPC on sample **A**. In this scan the QPC is set to the second conductance plateau, so that the signal shown in Fig. 3.2(b) is $\Delta G = (I_{SD}/V_{SD}) - 4G_0$.

Panels (a) and (b) of Fig. 3.2 show the characteristic electron branching. Branches extend over a length scale of about 5 μm due to the high mobility of the 2DEG. The fringes decorating these structures are separated by half the Fermi wavelength, consistently with the results of Ref. [48]. This can be better seen in Fig. 3.2(c), which shows a zoom-in on one of the branches. The inset shows a high-resolution image of the area indicated by the dashed rectangle. The interference fringes between time-reversed electron paths are clearly resolved. The interferometric nature of such structures can be easily verified by breaking the time reversal symmetry: when a small magnetic field (1 mT) is applied, all fringes are washed out (see Fig. 3.2(d)). As already pointed out by Aidala *et al.* [50], the magnetic field also affects the

[1] Details of the nanofabrication process are given in Appendix C.

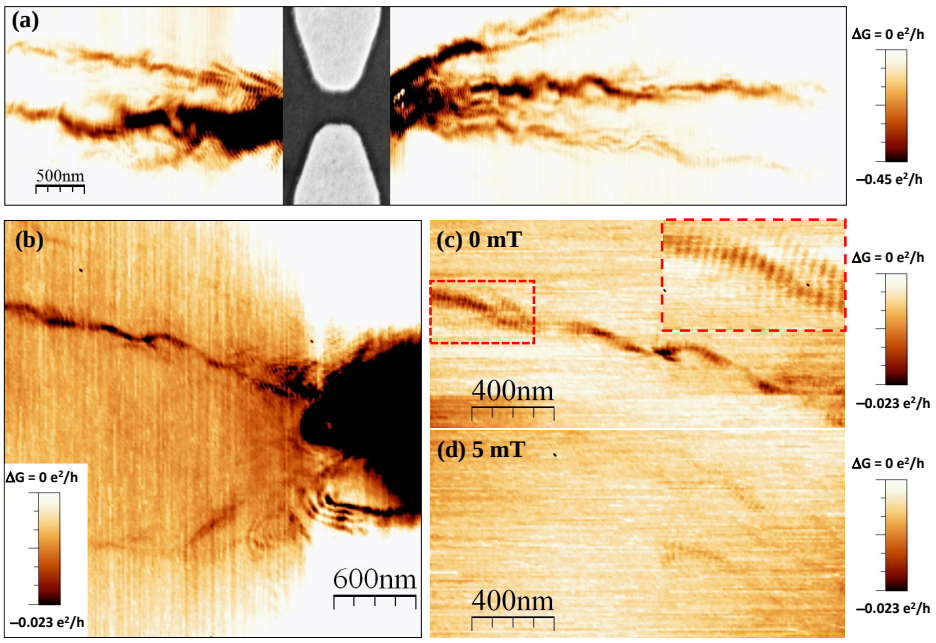

Figure 3.2: (a) Characteristic branched flow observed in zero-field SGM measurements (tip bias $V_{tip} = -5$ V, QPC transmission $G_T = 6G_0$) on sample **B**. The image shows the change in conductance ΔG as a function of tip position. The dark regions in the color plot (low conductance) correspond to the actual electron paths and depend on the details of the local potential. The fringes which decorate the branches are a signature of the electron phase coherence. The center part of the image shows a scanning electron microscopy image of the QPC. (b) SGM scan on sample **A**. The scan was performed on the left side of the QPC, that was set to the second conductance plateau. The two-lobe structure near the QPC is due to the presence of a quantum dot. (c) High-resolution image of the upper-left branch in panel (b). The inset shows a magnified image (500 nm$\times$ 300 nm) of the area indicated by the dashed rectangle. (d) The same scan has been repeated applying a small magnetic field (5 mT). The breaking of the time-reversal symmetry destroys both the branches and the fringes observed for zero field.

electron-flow pattern: electrons can no longer return to the QPC in a time-reversed path, and therefore the SGM image shows constant conductance, independently of tip position.

SGM scans are also sensitive to the presence of charge islands near the QPC that behave as quantum dots. Such islands are portions of the 2DEG that become isolated when the electrostatic confining potential of the QPC is increased relatively to the Fermi level. Such islands provide an additional channel for electron transmission. The effect of the tip is the same as that of a plunger gate in quantum dot devices [51]. Since the change in the

electrostatic potential induced by the tip on the dot depends on the tip-dot distance, the effect of Coulomb-blockade oscillations of the dot manifests itself as concentric rings in SGM maps.

3.3 Measurements in the integer QH regime

The possibility to bring the QPC into the QH regime opens the way to the investigation of novel features. In particular, the same device used to observe branched electron flow was exploited to implement a selector for edge channels, while the SGM tip was used to control their trajectory and backscattering probability. The idea of this experiment is sketched in Fig. 3.3. The bulk filling factor was set to $\nu_b = 4$ ($B = 3.125$ T, $\hbar\omega_c = 5.4$ meV). At this magnetic field the Zeeman gap is so small that we cannot clearly resolve spin-split edge channels. We shall thus neglect the spin and consider pairs of spin-split edges as individual channels carrying $2G_0$ units of conductance. The upper (lower) split-gate is negatively biased in order to set the underlying filling factor to g_u (g_l). The tip potential can be used to shift the edge position, tune the separation between the counter-propagating edge channels, and enhance backscattering.

We performed SGM measurements in different edge channel configurations. For instance, when the gate filling factors are set to $g_i = 0$, both edge channels reach the QPC center, while for $g_i = 2$, only one channel is deflected, whereas the other one propagates undisturbed under the gate.

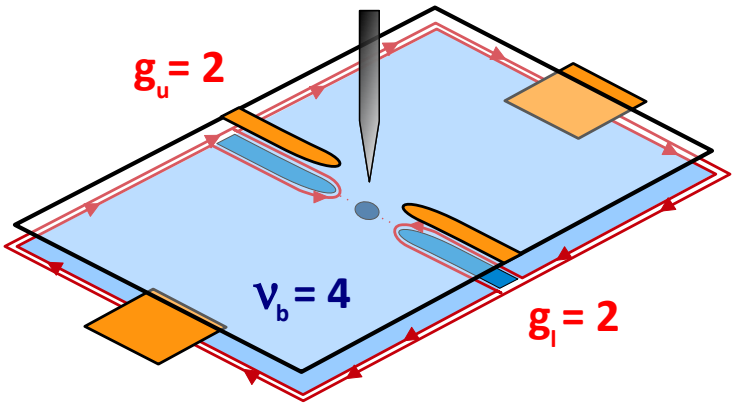

Figure 3.3: Sketch of the experiment. For bulk filling factor $\nu_b = 4$, the source-drain current is carried by two pairs of spin-degenerate edge channels, that can be selectively sent to a QPC by means of split-gates. The negatively-biased tip allows to tune the interaction between the counter-propagating edges. SGM maps are obtained by acquiring the source-drain conductance value at each tip position.

There are four (g_u, g_l) configurations of interest for our SGM measurements. Figure 3.4 shows the conductance map as a function of the position of the biased SGM tip ($V_{tip} = -5$ V) for each (g_u, g_l) combination. Since in these measurements the scan area overlaps the split-gates (whose position is indicated by the dashed grey line in Fig. 3.4), we increased the tip height to 30 nm to avoid tip-gate shorts.

Figure 3.4(a) refers to gate–region filling factors $g_u = g_l = 0$. For large tip-constriction distances the SGM signal reaches the full transmission value $4G_0$ (where $G_0 \equiv e^2/h$). When the biased tip is brought close to the QPC, pairs of edge channels are backscattered one by one, and the conductance through the QPC decreases in a step–like manner to 0. This demonstrates the gating action of the tip in the QH regime. Similar results were observed by Aoki et al. [46] in InAlAs/InGaAs etched heterostructures with a symmetric-edge configuration. Panels (b), (c), and (d) of Fig. 3.4 show the same measurement repeated for gate configurations (g_u, g_l) set to (0,2), (2,0), and (2,2), respectively. In (b) and (c), one of the two edge channels, rather than being sent to the QPC center, propagates under the split-gate along the mesa boundary. These scans demonstrate that it is impossible to backscatter more than one quantum of conductance (here $2G_0$) when only one channel is present at the counter-propagating edge. After the first edge is backscattered, conductance does not decrease anymore. The conductance is thus constant in the whole central region, exactly as expected when $g_u = g_l = 2$ (panel (d)).

As already discussed, the small value of the Zeeman energy does not allow to resolve spin-split edge channels, i.e. to observe a well-defined plateau at $G_T = nG_0$, with n an odd integer. One can nevertheless identify traces of the spin-splitting by observing the cross sections in Fig. 3.4, which show shoulders for $G_T = G_0$ and $G_T = 3G_0$.

The crucial result of this experiment is the clear and well-resolved observation of a plateau in the G_T map. Such a feature is strictly related to the reconstructed edge structure. In order to elucidate this point, we show in Fig. 3.5 the self-consistent energy dispersion within the QPC. In panel (a), the confinement potential is wide enough to allow full transmission: the filling factor at the QPC center is the same as in the bulk, i.e. there is an incompressible phase separating the two counter-propagating channels. Electron backscattering is thus suppressed. It can be "switched on" if tunneling between counter-propagating *compressible* stripes (A and C in Fig. 3.5(a)) is enabled. To this end, it is necessary to reduce the width of the QPC potential, until the compressible stripes merge at the center (Fig. 3.5(b)). If the QPC potential width is further reduced, the central compressible region shrinks and the backscattered current accordingly increases. When the width of the compressible region is reduced to zero, an incompressible phase occurs at the QPC center, which separates the two counter-propagating edges. Backscattering is again suppressed, so that a

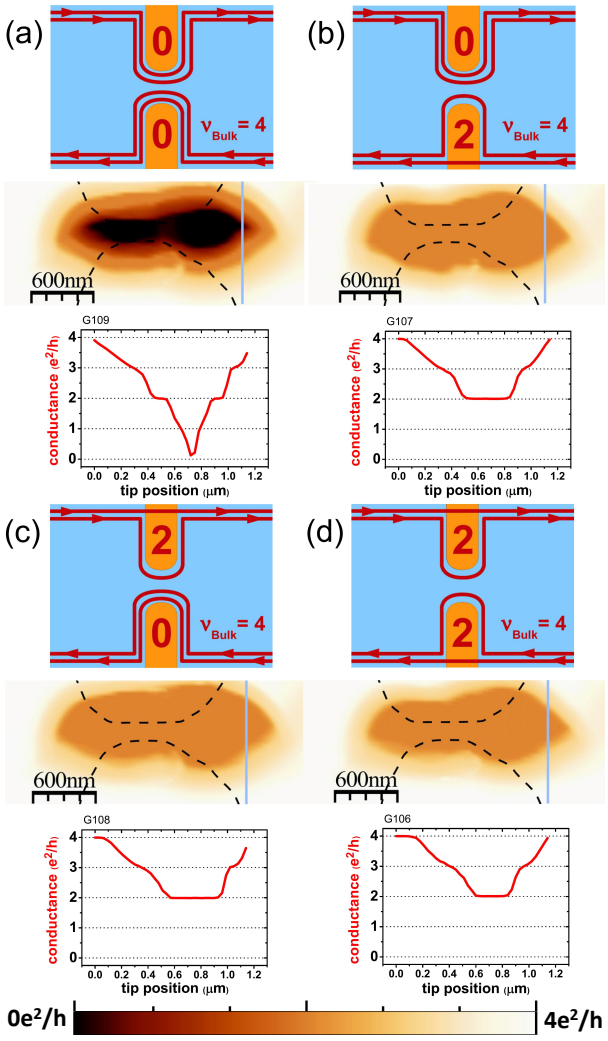

Figure 3.4: QPC conductance G_T as a function of the position of the biased SGM tip. The (bulk) 2DES filling factor is set to $\nu_b = 4$ (2 spin–degenerate edge channels; $B = 3.04$ T) while the QPC gates partially or completely deplete the 2DES underneath. The gate–region filling factors are $(g_u, g_l) = (0, 0)$ in (a), $(0, 2)$ in (b), $(2, 0)$ in (c), and $(2, 2)$ in (d). The top row shows sketches of the edge channel trajectories, the center row the SGM conductance images, and the lower row cross sections through the images along the vertical lines drawn in the images. The QPC outline as measured by AFM is indicated by the dashed lines.

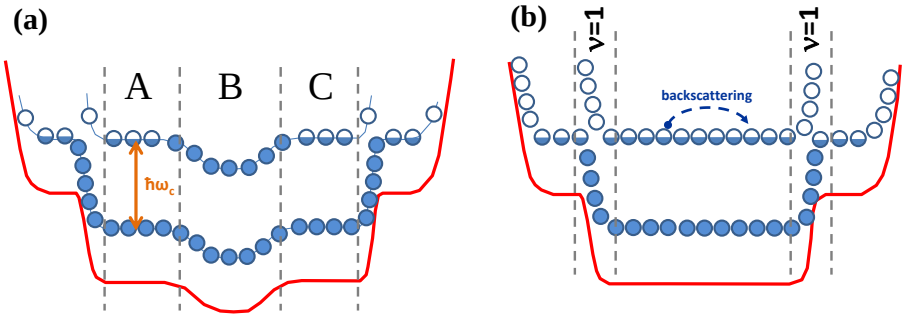

Figure 3.5: (a) Self-consistent edge dispersion in the QPC. The existence of an incompressile phase (B) at the QPC center prevents electron backscattering. (b) When the constriction is shrunk, two counter-propagating compressible stripes (A and C) merge at the center, so that backscattering is enabled. The width of the QPC potential can be reduced either by decreasing the split-gate voltage, or by moving the negatively-biased SGM tip.

plateau in the conductance is observed until we merge the next two adjacent compressible stripes. The width of the measured conductance plateau correspond to *twice* the incompressible stripe width δ_{IS}, as discussed in detail in Appendix B.

The QPC potential width can be reduced either by decreasing the split-gate voltage, or by moving the negatively-biased SGM tip. The advantage of the latter method is twofold: on the one hand, it allows to directly relate the spatial extent of the edge stripes with the plateaus in the SGM maps, on the other, it allows to exploit a statistical analysis to emphasize the presence of conductance plateaus. Such analysis consists in counting the occurrence of each value of G_T in the SGM map and plotting it in a histogram. The presence of a plateau implies that the corresponding G_T value is found more often in the SGM image, and therefore a peak is observed in the histogram. The histogram analysis of the SGM map of Fig. 3.4(a) is shown in Fig. 3.6. The occurrence of extremely sharp peaks for even filling factors demonstrates the validity of this analysis method. Histograms also provide a clear and reproducible way to estimate the plateau width. To this end, we selected the range of G_T values that are located within the FWHM of each peak in the histogram. The regions in the SGM maps, whose corresponding G_T values lie within this range, belong to the plateau. Plateau widths are thus obtained by taking the average width of such regions. This method can only be applied to plateaus with $0 < G_T < \nu_b G_0$. In fact, the plateaus corresponding to $G_T = \nu_b G_0$ and $G_T = 0$ indefinitely extend in the bulk 2DEG and in the depletion region, respectively. By applying this method to the scan in Fig. 3.4(a) we obtain $2\delta_{IS} = 42$ nm.

In order to compare these values with the predictions of the reconstruc-

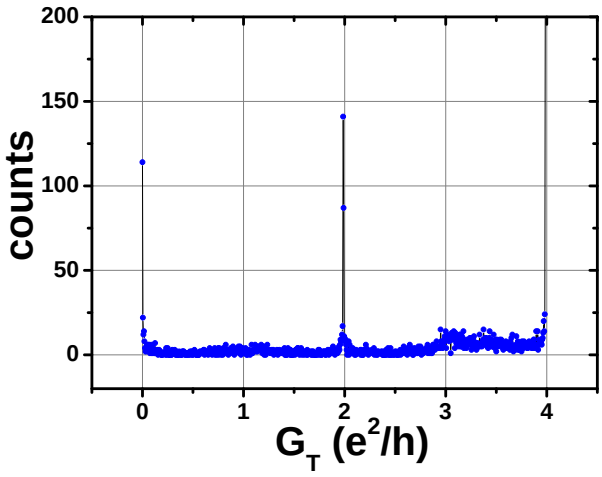

Figure 3.6: Histogram of the occurrences of each G_T value in the SGM image of Fig. 3.4(a). Peaks in the histogram emphasize the presence of plateaus at specific values of G_T. The peak width defines a range of G_T values, which corresponds to the plateau width.

tion picture, however, it is necessary to estimate the local electron density gradient close to the IS. In the reconstruction picture, the square of the width of the IS is proportional to the energy gap between the edge states and inversely proportional to the gradient of the electron density function. SGM scans allow to estimate the latter value by measuring the slope of G_T near the plateaus. In fact, when the tip is *near* a plateau, it induces a *compressible* phase at the QPC center, whose local filling factor is $\nu_c = G_T/G_0$. We are interested in determining dn/dr, where n is the electron density, and dr is the increment along the radial coordinate, which corresponds to one half of the tip displacement $\delta r_t = 2dr$. Therefore we have

$$\frac{dn}{dr} = \frac{n_L \delta\nu_c}{\frac{1}{2}\delta r_t} = 2n_L \left(\frac{1}{G_0}\frac{\delta G_T}{\delta r_t}\right), \tag{3.1}$$

where n_L is the Landau level degeneracy, and the quantity in brackets is the slope of G_T in the SGM maps.[2] By inserting the electron-density gradient and the LL gap ($\hbar\omega_c = 5.4$ meV) in Eq. 1.9 we obtain a plateau width $2\delta_{IS} = 2 \times 28$ nm=56 nm. The agreement with the value directly extracted from the SGM scan is good, and validates the approximations made.

Figure 3.7(a) shows a SGM measurement on another device (sample **A**) at bulk filling factor $\nu_b = 6$ ($B = 1.22$ T). The tip and the split-gate bias are set to $V_{tip} = -3$ V, and $V_g = -0.35$ V, respectively. In this case, when

[2]The method we used to extract this quantity from the SGM maps is described in detail in Appendix B.2.

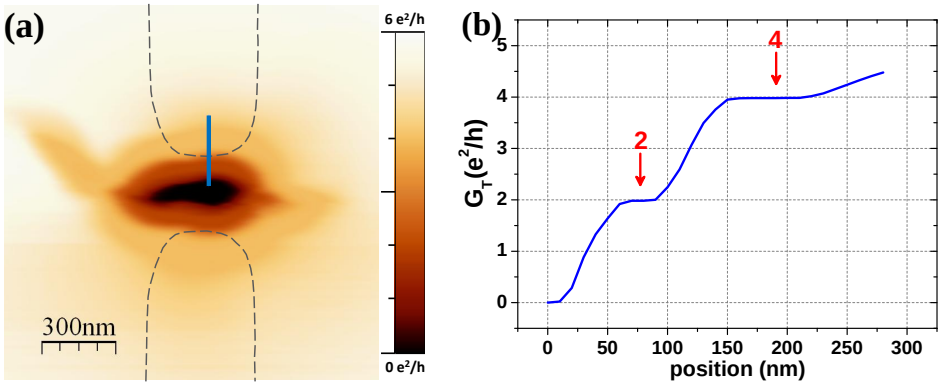

Figure 3.7: Map of the source-drain zero-bias conductance G_T as a function of the position of the tip with respect to the split-gate (dashed line), in a QH system at $\nu_b = 6$. When the biased tip ($V_{tip} = -3$ V) approaches the QPC center, individual channels are selectively backscattered, and a series of compressible/incompressible stripes becomes visible.

the split-gate filling factors (g_u, g_l) are set to (0,0), *two* finite plateaus are visible.

Figure 3.7(b) displays the conductance curve corresponding to the light blue line in Fig. 3.7(a). This plot clearly demonstrates the presence of plateaus when G_T equals multiples of $2G_0$. In this case, the resulting plateau widths are $2\delta_{IS} = 15$ nm for $G_T = 2G_0$ and $2\delta_{IS} = 42$ nm for $G_T = 4G_0$. The predictions of the reconstruction model [10] are $2\delta_{IS} = 32$ nm and $2\delta_{IS} = 47$ nm, respectively. While the latter turns out to be in good agreement with the measured value, the former is rather larger. This difference might be explained by considering that the IS width in this case is not negligible with respect to that of the two neighboring compressible stripes, in contrast with the fundamental assumptions made in Ref. [10].

3.4 Imaging fractional stripes in integer channels

The existence of fractional order within integer QH systems is suggested by a number of transport measurements. These indications led Beenakker to model the integer edge as if composed by a set of independent edge channels that can be selectively populated and detected. This behavior was at odds with the first edge models proposed by Halperin [11], where every integer Landau level in the bulk gives rise to a chiral edge mode which has no internal structure and can be described in terms of single-particle physics. The missing ingredient – electron-electron interaction – enters as a quite complex agent within this context: it can lead to non-perturbative effects, such as the emergence of fractional QH edge substructures, as suggested by Beenakker [28]; it is known to perturb the edge profile due to gap – and thus

density – dependent screening effects which lead to extended compressible and incompressible stripes, as shown by Chklowskii [10].

Despite the many experimental and theoretical studies, the key issue of fractional order within integer QH systems has not been clearly settled yet. While a number of experiments showed clear indications of fractional phases in constrictions, either in terms of fractional quantization of conductance [3, 4] or Luttinger-like non-linear features [24–27], many issues remain open, and even the simple problem of how an ideal integer edge might "branch" and give rise to fractional edges remains unclear. Notably, recent experiments of interferometry [6] and out-of-equilibrium energy spectroscopy [52] demonstrated that an integer edge can behave as a monolithic object with no evidence of an inner structure. Whether such dual behavior depends on the specific device structure or is intrinsic, remains an unanswered question. Finding experimental indications is complicated by the fact that fractional features are often difficult to spot in a clear way, due to the inevitable random variability of real devices: fractional conductance quantizations steps, for instance, can be easily masked by disorder or resonances.

In the previous section we saw that SGM measurements on QPCs are a valuable tool to observe the spatial details of integer edge channels with rather high resolution, compared to other scanning probe techniques. In this section we show how the same setup can be exploited to reveal fractional structures within a single integer channel. The visibility of such structures critically depends on sample quality, so that they could not be observed in previous SGM experiments performed with samples with lower mobility (InAlAs/InGaAs) [46]. The devices used in this experiment are fabricated starting from two heterostructures: sample (**C**) has a 2DEG depth $D_C = 80$ nm, a carrier density $n_C = 1.99 \times 10^{11}$ cm^{-2}, and a dark mobility $\mu_C = 4.5 \times 10^6$ cm^2/Vs. The corresponding values for sample (**D**) are $D_D = 100$ nm, $n_D = 2.11 \times 10^{11}$ cm^{-2}, and $\mu_D = 3.88 \times 10^6$ cm^2/Vs.

Figure 3.8(a) shows a SGM measurement on a QPC on sample **C** in the QH regime at bulk fillig factor $\nu_b = 1$ ($B = 8.23$ T). The split-gate voltage is set to $V_g = -0.30$ V, which allows to set the filling factor underneath to $\nu = 0$ without inducing backscattering between the counter-propagating edges inside the constriction (transmission of the QPC $t = 1$). Figure 3.8(a) is a map of the transmitted source-drain differential conductance G_T as a function of the tip position, with a bias $V_{tip} = -6$ V applied to the tip. Similarly to the scans shown in Fig. 3.4 and 3.7, when the distance between tip and QPC center is gradually reduced, backscattering is enhanced and G_T decreases. This measurement is aimed at searching for the occurrence of fractional incompressible phases, that should show up as plateaus in the SGM scans, exactly as for the integer IS. On the right side of Fig. 3.8(a), we show a blow up of the 50 nm×150 nm region corresponding to the dashed rectangle. From the contour-line density we can recognize a shoulder cor-

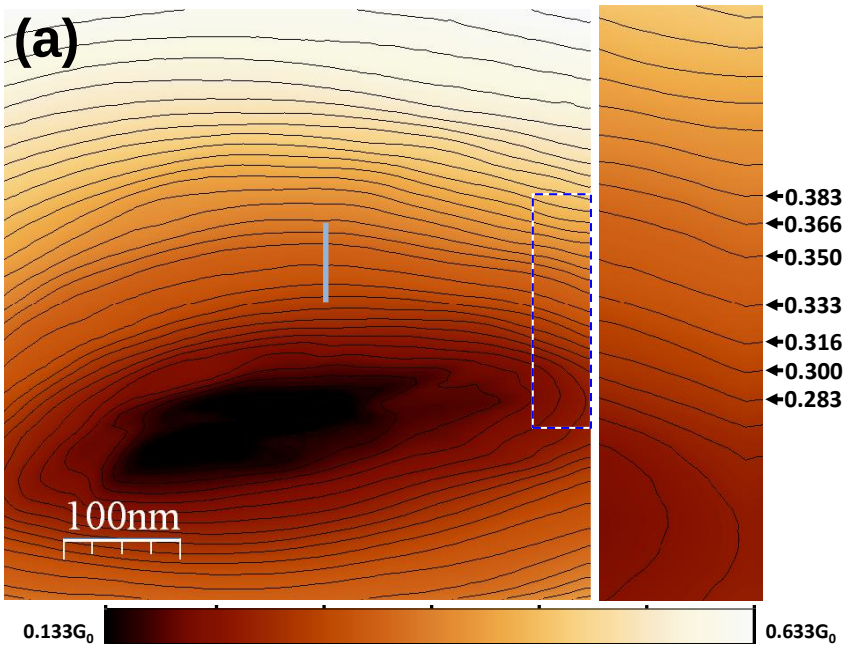

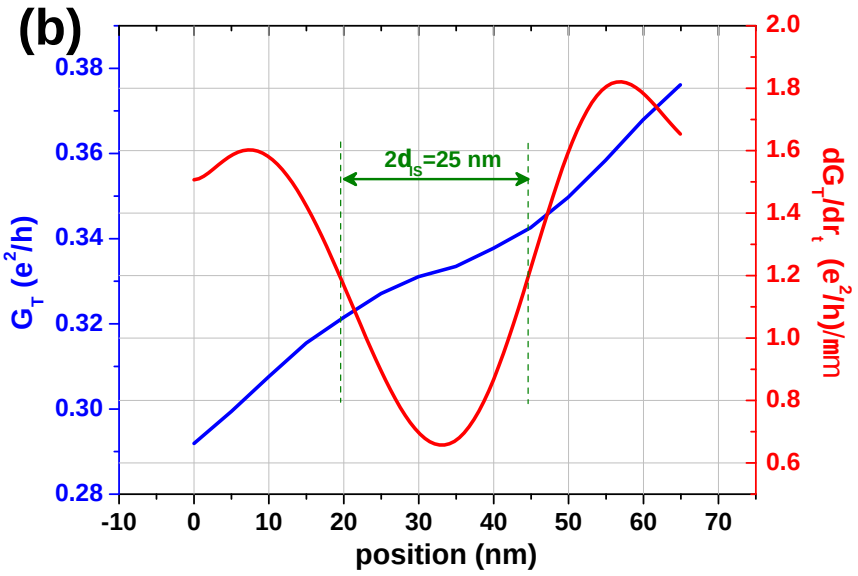

Figure 3.8: (a) SGM scan at the center of a QPC in a $\nu_b = 1$ QH system. The map shows the G_T values as a function of the tip position, together with contour lines at constant G_T. On the right, a zoom of the 50×150 nm region corresponding to the dashed rectangle is displayed. (b) Profile of G_T along the light blue line in (a), together with its derivative.

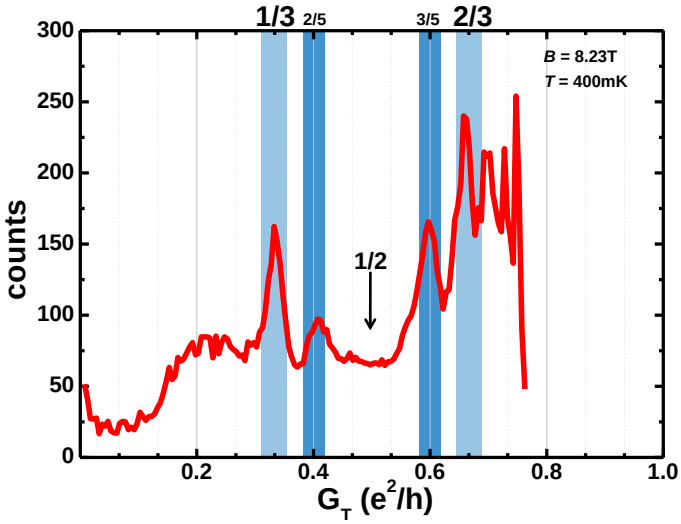

Figure 3.9: Graph of the average occurrence of each G_T value within 9 different SGM scans performed at different V_{tip} values. Peaks for $G_T = 1/3$, 2/5, 3/5, and 2/3 are visible.

responding to a plateau for $G_T = 1/3G_0$. This plateau can be directly observed in Fig. 3.8(b), where we show the conductance profile acquired along the light-blue line in Fig. 3.8(a), together with its derivative. From the half-width of the minimum in the derivative we can estimate the width δ_{IS} of the fractional IS and obtain approximately 12 nm.

Figure 3.9 shows the graph resulting from the averaging of 9 histograms extracted from SGM scans performed at different tip voltages (V_{tip} from -7.5 to -3.5 V). Peaks for $G_T = 1/3$, 2/5, 3/5, and 2/3 are clearly visible. Such values correspond to the most relevant fractions (1/3 and 2/5) together with their symmetry conjugates (2/3 and 3/5). Similar measurements were performed on six samples, and at least the 1/3 peak was always clearly visible. The amplitude of the different peaks reflects the relative robustness of the fractions, e.g. in Fig. 3.9 the 1/3 peak is three times larger than the 2/5 peak. The averaging procedure allowed us to sample the whole conductance range from 0 to $2/3G_0$. In fact, in scans with high V_{tip}, the higher G_T values lie outside the scan area. Vice-versa, in scans with low V_{tip}, G_T is higher than $2/5G_0$ even at the QPC center. SGM scans allow to greatly enhance even weak structures because they provide much more information than a single sweep of the split-gate potential. Even though weak structures cannot be easily recognizable in a single sweep, they become evident in a histogram graph, where all spurious structures are averaged out. It is also important to notice that the ability to resolve thin stripes is due to the high spatial resolution provided by the SGM technique, compared to scanning force or scanning capacitance microscopy [39, 42–44, 53, 54]. As discussed

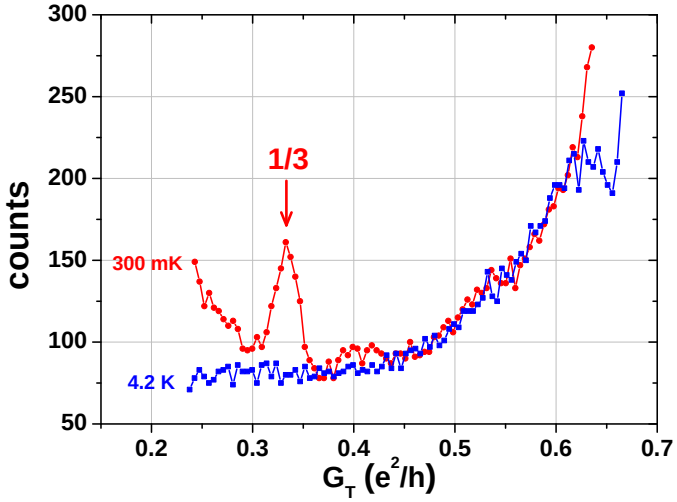

Figure 3.10: Plots of the occurrences of G_T values for two SGM scans performed at 300 mK (red curve) and 4.2 K (blue curve), on a QPC fabricated on sample **C**. The increase of temperature completely washes out the fractional IS, so that the 1/3 peak disappears.

in detail in chapter 2, here the resolution is only related to the accuracy of the piezo scanner that controls the tip-sample position, which is of the order of 0.1 nm. Even though the width of the electrostatic potential induced by the tip is relatively large (typically more than 100 nm), what matters here is how accurately the equipotential contour is moved, i.e. the precision of the lateral displacement of the edge.

Figure 3.10 shows the impact of temperature on the visibility of fractional peaks, measured on a QPC fabricated on sample **D**. While at 300 mK a peak for $G_T = 1/3G_0$ is clearly observed, at a base temperature of 4.2 K the 1/3 peak completely disappears, and the curve become featureless. This is consistent with the picture of an incompressible stripe originating from the condensation of fractional quasi-particles with an excitation gap $\Delta_{1/3}$ of the order of 1 K (≈ 100 μeV), as estimated from tunneling measurements on samples with similar characteristics [27]. This value is also consistent with recent magnetocapacitance experiments [55] that measured a chemical potential jump across the fractional gap of the order of $\Delta\mu_{1/3} = 3\Delta_{1/3} \approx 400$ μeV at 0.5 K. The fractional gap is rapidly suppressed as the temperature increases [55], so that at 4.2 K almost all the quasi-particles are excited, therefore screening is effective and compressibility increases.

As discussed before, the histogram in Fig. 3.9 allows to define the range of values of G_T which correspond to a certain plateau by taking the FWHM of each peak. These intervals of G_T correspond to a stripe in each SGM map, whose average width is a good approximation of the fractional plateau width. By applying this procedure to all SGM scans, we can extract the

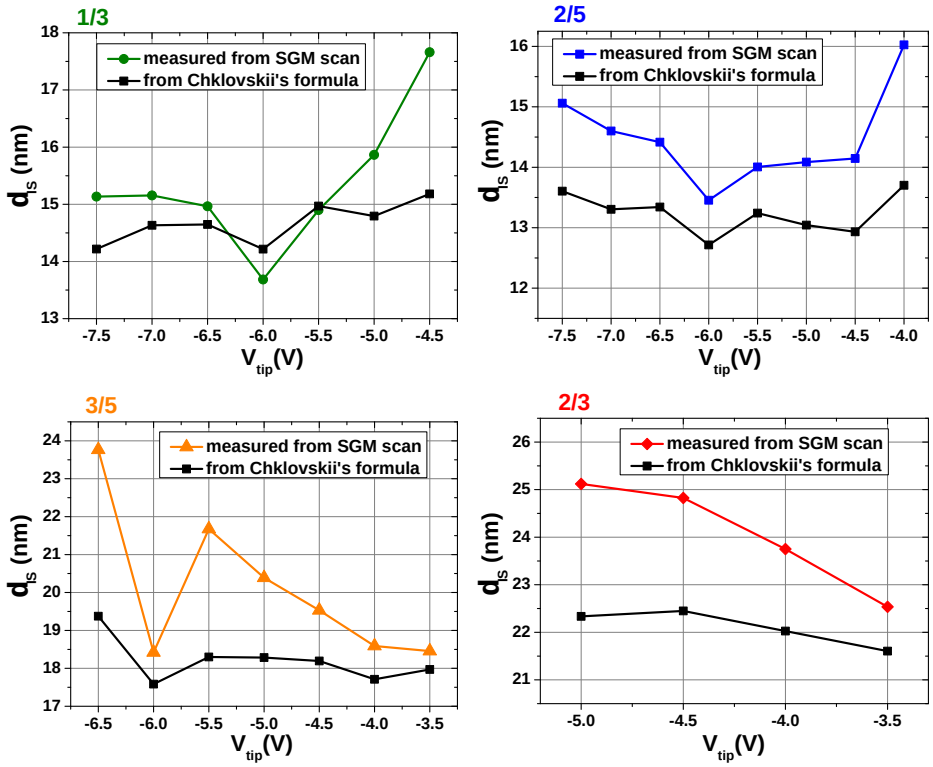

Figure 3.11: For each fraction reported in this section, we show δ_{IS} measured for different V_{tip} values (color spots) together with the values expected from Chklovskii's formula assuming $\Delta\mu_f = 260$ μeV (black squares).

value of δ_{IS} of each fractional IS. These values are consistent with those obtained from a direct estimate of the plateau width (see Fig. 3.8(b)). In order to compare these values with the predictions of the reconstruction picture, we used the method discussed in Sect. 3.3 for the integer IS case. We estimated the electron density gradient by Eq. 3.1 and we inserted it in Eq. 1.11. Figure 3.11 shows, for all the observed fractions, a comparison between the values directly extracted from the SGM map and those deduced from Eq. 1.11, for each value of V_{tip}. Both the absolute values and the trends of the reconstruction model predictions are in good agreement with the experimental data.[3] This supports our analysis method and allows us to convert tip-voltage into a universal electron density gradient scale. In Fig. 3.12 we report all measured δ_{IS} as a function of the electron density gradient, together with the predictions of Chklovskii's formula (Eq. 1.11) for $\Delta\mu_f = 200$, 300 and 400 μeV (black lines). The agreement between the data and the reconstruction model is excellent, especially in light of

[3]For further information see Appendix B.

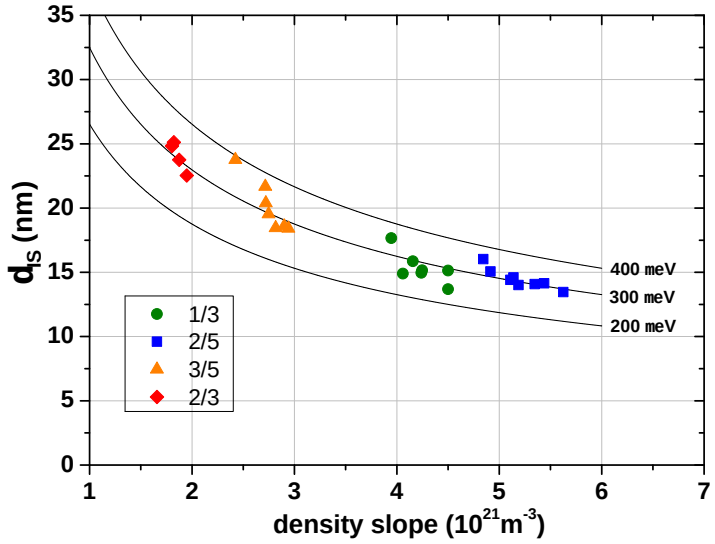

Figure 3.12: IS width δ_{IS} plotted as a function of the electron density gradient (scatter plots), together with the reconstruction picture predictions for $\Delta\mu_f = 200$, 300 and 400 μeV (thin lines).

the uncertainty on the fractional-gap, which is known to be rather sensitive to the details of the disorder potential. Notably, data globally follow the expected $(dn/dr_t)^{-1/2}$ dependence.

Our results convincingly demonstrate the occurrence of IS at the sample edge where the filling factor equals the most robust fractional states. Such IS are wider than the magnetic length ($\ell = (\hbar/eB)^{1/2} = 9$ nm) and can effectively isolate the compressible stripes in between. This explains why the fractional components behave as independent channels that can be selectively populated and detected [3, 4, 28, 56]. The presence of fractional IS also explains the observation of Luttinger liquid behavior in tunneling experiments between $\nu = 1$ phases (Fermi liquids), presented in Ref. [27]. Such results were interpreted by assuming that electrons tunnel through a region with local fractional filling factor ν^* separating the two main incompressible phases at $\nu = 1$. Our work shows that such a region is precisely the fractional IS that is present at the sample edge. In other words, the QPC in Ref. [27] was used to individually select the fractional components within an integer edge.

Chapter 4

Coherent edge-channel mixing controlled by SGM

In the previous chapter we showed how the SGM can be used to probe with unprecedented resolution the inner edge structure, i.e. the local electron density, group velocity, and compressibility function across the channel. The present chapter shows that the SGM tip can be used not merely as a probe, but also as an *active component* of a complex device in which one can address quantum structures whose dimensions are continuously tuned by appropriately positioning the biased tip of the SGM. The movable tip introduces a new degree of freedom for transport experiments, since it allows to continuously control the size of a single component of the device under investigation during the same low–temperature measurement session. In this specific case, we exploited this ability to investigate the scattering mechanisms that allow to transfer electrons between two co-propagating edge channels.

4.1 Spatially resolved analysis of edge-channel equilibration

It is probably not immediately clear why a SPM technique should be necessary to study scattering between parallel edge channels. Charge transfer and electro–chemical potential imbalance equilibration can be studied by transport measurement, as shown by several groups [57–61]. In these experiments, two co–propagating edge channels originating from two ohmic contacts at different potential meet at the beginning of a common path of fixed length d, where charge transfer tends to equilibrate their voltage difference [60]. At the end of the path the edge channels are separated by a selector gate and guided to two distinct detector contacts. Consequently, these setups yield information on the *cumulative* effect of the processes taking place along the whole distance d. Very little can be said about the

microscopic details of the inter-channel scattering process. In particular, it is still not clear either what are the relevant sources of scattering, or to what extent such processes are coherent.

Clearly, to address these questions, a spatially resolved investigation is needed. This is precisely the goal of our SGM experiments. To face this task, we designed a special QH circuit where the interaction distance d between two imbalanced edge channels is tip-position dependent, as sketched in Fig. 4.1. The inter-channel scattering is revealed by measuring the current of the two output edge channels, I_A and I_B. The ability to tune d with continuity makes it possible to probe the role of a local detail at position x by simply observing any *change* in the scattered current for $d = x$.

Our size-variable QH circuit was defined on sample **E** by using the electro-static potential generated by three gates *and* the SGM tip. The upper left gate in Fig. 4.1(b) defines a region with local filling factor $g = 2$ which selects only one of the two channels propagating from contact 1 at voltage V and guides it towards contact 2. When this is grounded, an imbalance is established between edge channels at the entrance of the constriction defined by the two central gates at local filling factor $g = 0$. The two channels propagate in close proximity along the constriction, which is 6 μm long and 1 μm wide (lithographically). In our experiments, we tuned the depletion spot induced by the biased tip of the SGM so that the inner channel is completely backscattered, while the outer one is fully transmitted. As a consequence, the two channels are separated after a distance d that can be adjusted by moving the tip. Since the outer edge was grounded before entering the constriction, the detector contact B will measure only the electrons scattered between channels, while the remaining current is detected at contact A. Experiments were performed on many samples: in particular, the data reported in this chapter refer to measurements performed on two nominally identical devices, labeled #**E1** and #**E2**.

The peculiar geometry of this QH circuit implies that all measurements critically depend on the ability to set the edge configuration so that the inner edge is perfectly reflected while the outer one is fully transmitted. To this end, we first performed topography scans (Fig. 4.2(a) shows data relative to device #**E1**), that yielded a reference frame to evaluate the relative position of the tip with respect to the confining gates in the subsequent SGM scans. Then, we performed calibration scans aimed at establishing tip trajectories ensuring that the inner channel is indeed completely backscattered, while the outer one is fully transmitted (edge configuration as sketched in Fig. 4.1). In these scans, a small AC bias ($V = 50$ μV) was applied to source contact 1, while contact 2 was kept floating, so that both channels at the entrance of the central constriction were at the same potential and carried the same current $I_1 = I_2 = 2G_0V$. In this sense, this measurement is analogous to that reported in Fig. 3.4(a). Again, by moving the tip towards the axis of the 1D–channel, the inner edge channel is increasingly backscattered and the

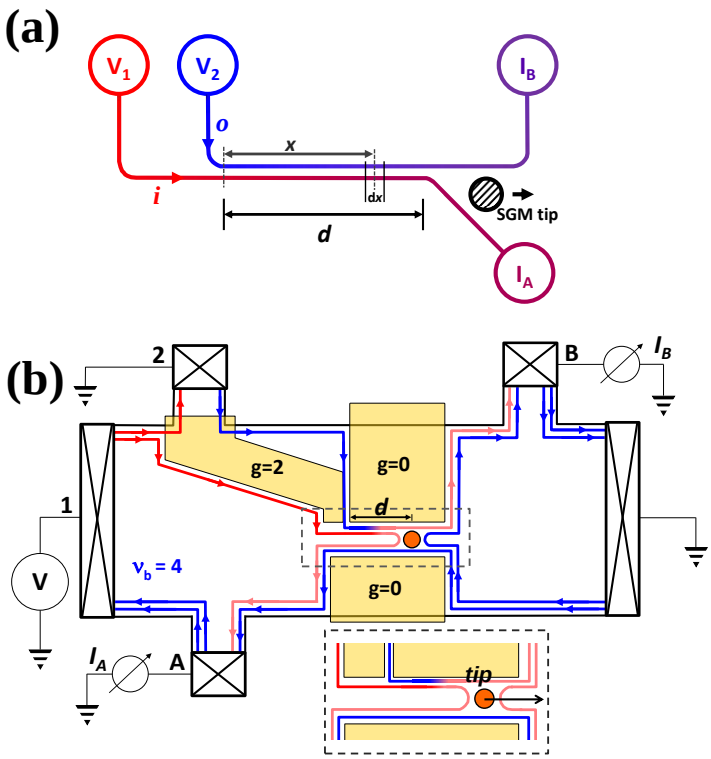

Figure 4.1: (a) Schematic drawing of the key idea behind our experiment: the SGM tip is used to actively control the edge trajectories to obtain a continuously tunable interaction region length d. This allows a spatially resolved analysis of the equilibration process. (b) Scheme of the experimental setup. Three Schottky gates are used to independently contact two co-propagating edge channels and to define a 6-μm-long and 1-μm-wide constriction. Using the SGM tip it is possible to selectively reflect the inner channel and to define a variable interedge relaxation region length d.

conductance decreases until we reach a plateau for $G_B = 2G_0$ (left panel of Fig. 4.2(c)). Thus the tip trajectory ensuring the desired edge configuration (as depicted in Fig. 4.1(b)) was determined as the set of the middle points of the plateau stripe (blue line in Fig. 4.2(b)). As shown in the right panel of Fig. 4.2(c), the conductance along this trajectory is a constant and equals the conductance of a single channel, i.e. $2G_0$.

Next, we imaged the inter–channel differential conductance. The two edge channels entering the constriction were imbalanced by grounding contact 2. In this configuration, at the beginning of the interaction path, only the inner channel carries a non–zero current, i.e. $I_1 = 2G_0V$, where V is the source voltage. The electrochemical potential balance is gradually restored by scattering events that take place along the interaction path, and this yields a partial transfer of the initial current signal from the inner to the

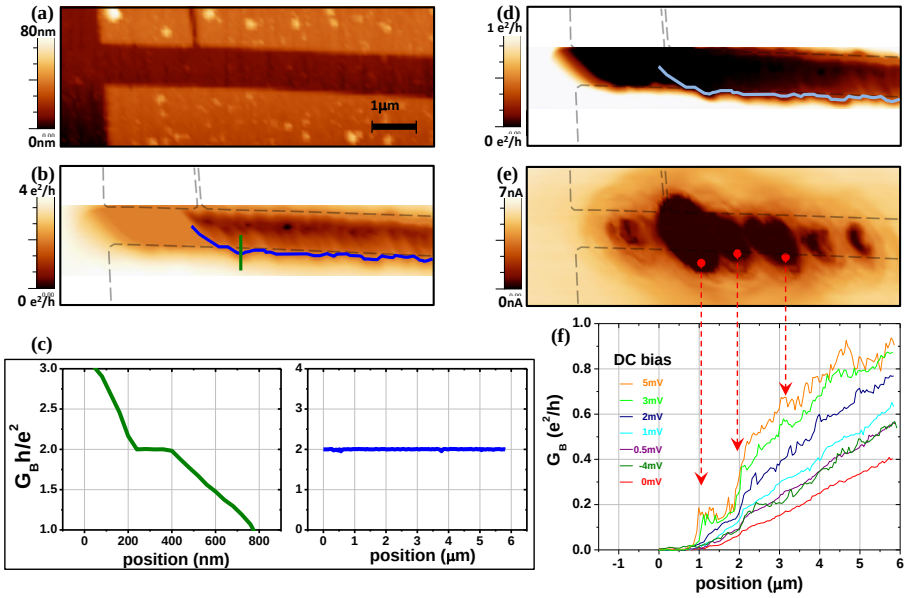

Figure 4.2: (a) Topography scan of device #**E1**. (b) Calibration scan: the SGM map refers to the differential conductance signal measured at contact B when contact 2 is floating. $V_{tip} = -10$ V. (c) Conductance profiles measured along the green (left panel) and the blue (right panel) line in (b). (d) Imaging of the inter–channel equilibration (contact 2 grounded). (e) SGM measurement at zero magnetic field, with DC source bias $V = 100$ μV. (f) Finite bias equilibration signal measured along the trajectory (blue line in Fig. 4.2(b) and (d)) determined by means of the calibration scan. There is a clear correlation between the steps in the equilibration curves and the position of scattering centers in the SGM scan at zero magnetic field. Furthermore, we observe an enhancement of the equilibration steps with increasing bias.

outer channel. The device architecture allowed us to detect both transferred electrons and reflected ones by measuring the current signal at contacts B and A, respectively. We verified that the sum of currents measured at A and B was constant and equal to $2G_0V$.

Figure 4.2(d) shows the SGM map of the inter–channel differential conductance G_B at zero DC bias. The key feature of this scan is the monotonic increase of the scattered current as a function of the interaction distance d. This can be directly observed in Fig. 4.2(f), where we show several finite–bias conductance profiles acquired along the trajectory (blue line in Fig. 4.2(b)) determined in the previous calibration step. For a given value of d, the increase of the equilibration for increasing DC inter-edge bias is consistent with the results obtained by means of I–V characteristics (as witnessed by the increasing G_B) in samples with fixed interaction length [60]. In particular, for DC bias of the order of the cyclotron gap, $\hbar\omega_c = 5.7$ meV,

the differential conductance reaches its saturation value $G_B = G_0$, which corresponds to a transmission probability $T_{12} = 0.5$, i.e. $I_A = I_B$.

All curves in Fig. 4.2(f) are characterized by sharp steps in some positions. This behavior was confirmed by measurements on other devices, which showed the same stepwise monotonic behavior albeit with different step positions. This indicates that the scattering probability is critically influenced by the local sample details, e.g. by the location of impurities that can produce sharp potential profiles whose effect in the QH inter–channel scattering can be revealed by the SGM technique [62]. In order to correlate the presence of scattering centers with the steps in the conductance profile we performed SGM scans at zero magnetic field (Fig. 4.2(e)). Such a scan provides a direct imaging of the disorder potential and can identify the most relevant scattering centers (see Refs. [48, 63] for similar scanning probe microscopy investigations). A comparison between Fig. 4.2(e) and Fig. 4.2(f) shows a remarkable correlation between the steps in the conductance profiles and the main spots in the disorder–potential map. This is the central finding of the present experiment and establishes a direct link between the atomistic details of the sample and the inter–channel transport characteristics. Such a correlation would be impossible to detect with standard transport measurements and requires the use of scanning probe microscopy techniques.

It is important to note that inter–channel transmission is nearly zero up to the first scatterer. This indicates that impurity–induced scattering is the dominant process equilibrating the imbalance, while other mechanisms that were invoked in literature, like acoustic–phonon scattering, have only a negligible effect for short distances, in agreement with the theoretical findings of Ref. [58]. We also observe that the step amplitude is suppressed when the length of the interaction path d is larger than about 3 μm.

In view of possible applications to QH interferometry, it is necessary to determine the degree of coherence of the position–dependent, inter–channel differential conductance. For this reason we developed a theoretical model[1] which accounts for elastic scattering only and restricted our analysis to the zero–DC bias case. The system is described through a tight–binding Hamiltonian, where the magnetic field is introduced through Peierls phase factors in the hopping potentials. According to the Landauer–Büttiker formalism [64, 65], the differential conductance is determined by the scattering coefficients which are calculated using a recursive Green's function technique. Apart from a hard–wall confining potential, electrons are subjected to a disorder potential consisting of few strong scattering centers on top of a background potential. Scattering centers are modeled by Gaussian potentials whose positions (which are different from device to device) are deduced

[1] This model has been implemented in collaboration with R. Fazio, V. Giovannetti, D. Venturelli and F. Taddei, of the QTI group at Scuola Normale Superiore.

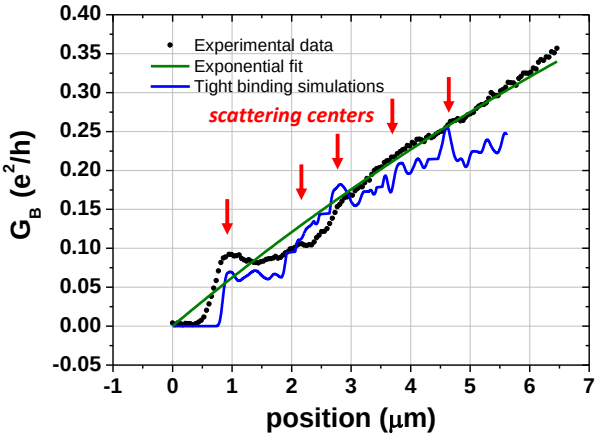

Figure 4.3: Results of the tight–binding simulations for the zero–bias case: the inter–channel, zero–temperature differential conductance (solid line) compared with experimental data from device #**E2** (filled dots). From the exponential fit (green line) we deduce an equilibration length $\ell_{eq} = 15$ μm. The position of strong scattering centers in the simulation is indicated by red arrows. Comparison of the curves in Figs. 4.2.(f) and 4.3 demonstrates that the position of the jumps changes from sample to sample and critically depends on the specific distribution of the scattering centers in each sample, which is the main finding of this experiment.

from SGM scans in the constriction at zero magnetic field (Fig. 4.2(e) shows one example). The height of the Gaussian potentials was chosen of the order of the cyclotron gap and their extension on a length scale of the order of the magnetic length ($\ell_B \approx 15$ nm). The background potential was modeled as a large number of randomly distributed smooth Gaussian potentials, whose height is of the order of one tenth of the cyclotron gap. The conductance was calculated averaging over a large number of random configurations of the background potential to account for phase-averaging mechanisms which are always present in the system.

Figure 4.3 shows results of our simulations (solid blue line), together with the experimental data from device #**E2** for $V = 0$ (filled black dots) and an exponential fit (green line). For short distances the computed conductance exhibits steps in correspondence to the scattering centers (positions indicated by red arrows in Fig. 4.3), while at larger distances a monotonic behavior is observed. Steps are washed out by the averaging over the background. Both regimes are consistent with the experimental data.

In Fig. 4.3 we also compare our experimental data with the exponential behavior $G_B = G_0(1 - e^{-d/\ell_{eq}})$ which was previously reported [57, 60]. For short d, there is a discrepancy between the experimental conductance profile and the exponential curve, due to the discreteness of the scattering

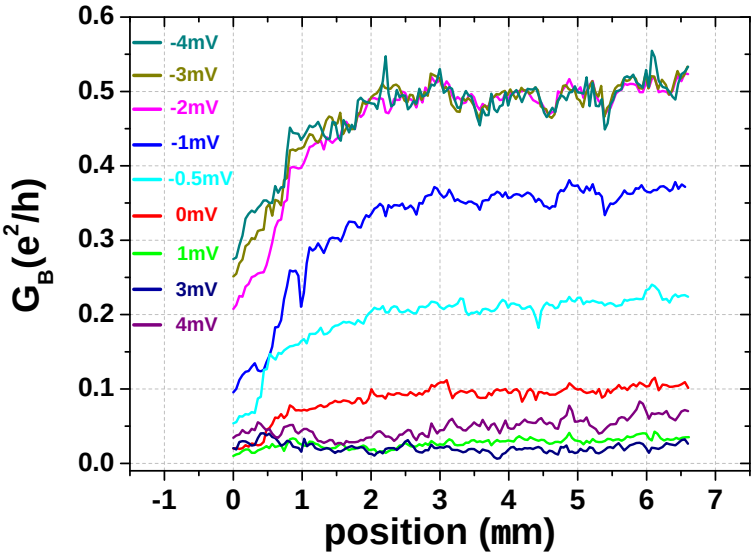

Figure 4.4: Inter-channel differential conductance as a function of the interaction distance d measured at bulk filling factor $\nu_b = 2$ on device #**E2**.

centers. On the other hand, for larger distances our experimental data are well fitted by the exponential curve. We should underline that here we can actually directly verify this exponential behavior, by continuously tuning the interaction length d. In previous works, the equilibration length ℓ_{eq} was extracted from four-wire resistance measurements at fixed d, *assuming* an exponential dependence [57, 58, 60, 66]. From our data we obtain an equilibration length $\ell_{eq} = 15$ μm, which is of the same order of magnitude of other values reported in literature [66].

Figure 4.4 shows the results of finite-bias measurements on device #**E2** performed at bulk filling factor $\nu_b = 2$, so that equilibration takes place between two spin-split edge channels. As shown in the graph, most of the charge is transferred for $d < 1$ μm, i.e. as soon as the two channels start interacting. For $d > 1$ μm the curves in Fig. 4.4 are flat, consistently with the fact that typical equilibration lengths reported in literature for $\nu_b = 2$ are of the order of millimeters [57]. Since the electron scattering between two spin-polarized edge-channels requires spin-flip, the disorder potential is not sufficient to induce transfer. Therefore the scattered current is only weakly depending on d. On the other hand, it appears to critically depend on the edge-channel imbalance. For large negative bias ($V < -2$ mV), complete equilibration ($G_B = 0.5\ e^2/h$) is achieved for $d \approx 1$ μm. In the next paragraph we shall focus on the non-linear regime and discuss how the current–voltage characterics depend on d.

4.2 Inter-channel equilibration in the non-linear regime

The measurement discussed in the previous section clearly evidenced that at low inter-edge bias the dominant equilibration process is elastic scattering induced by impurities. For bias exceeding the LL gap, however, radiative transitions are observed as well [67]. This effect was recently exploited to implement an innovative converter from phase-coherent electronic states to photons in the THz region [68]. While the occurrence of this radiative emission is well established, the interpretation of the threshold value is actually unclear. In fact, several papers showed [58, 60, 66, 68, 69] that the threshold voltage is considerably smaller than the nominal Landau level gap $\hbar\omega_c$. Some gap reduction mechanisms were suggested [60], but spectroscopic studies evidenced no deviation of the photon energy from $\hbar\omega_c$ [70]. Thus a convincing explanation for such a shift is missing so far.

The experimental setup discussed in the previous section can address this puzzle, since it is possible to follow the evolution of the threshold voltage when the interaction length d is varied. In fact, the first step to understand the nature of the threshold shift is to determine whether it depends or not on d, and if it does, how. Using the QH circuit shown in Fig. 4.1, we can measure the current-voltage (I_B-V_1) characteristics of the inter-channel charge transfer, for any value of the interaction distance d compatible with device dimensions, i.e. from 0 to 6 μm. In a sense, this measurement is complementary to the one reported in the previous section. Experimental data are shown in Fig. 4.5(a). The first relevant feature concerns the zero-bias differential conductance which monotonically increases with the interaction length d, as shown in Fig. 4.5(c). The curves are asymmetric around zero. While the scattered current displays a non-linear but featureless dependence on V_1 for positive bias,[2] we will focus on the analysis of the negative bias range ($V_1 < 0$, i.e. $\mu_i > \mu_o$), where a transition between two distinct linear regimes can be observed. Two linear curve sections with different slope are separated by a kink occurring at a threshold voltage V_{th}. We can estimate V_{th} for each individual curve by extrapolating straight lines for both the small bias and the saturation regime and taking the abscissa of the intersection point, as explicitly shown in Fig. 4.5(a) for the $d = 1.5$ μm curve. When the applied bias (V_1) is such that $|V_1| < |V_{th}|$, the junction resistance between the two channels increases when d is lowered. On the other hand, for $|V_1| > |V_{th}|$ the differential conductance saturates to $G_0 \equiv e^2/h$, i.e. half of the total conductance, so that an increase δV_1 of the input bias produces a voltage increase $\delta V_1/2$ in both output edges. In fact the resulting output current is $\delta I_B = G_0 \delta V_1$, and therefore $\delta V_B = (h/2e^2)\delta I_B = \delta V_1/2$. Thus,

[2] The analysis of this behavior is beyond the scope of the present thesis. It was already observed in other experiments [60].

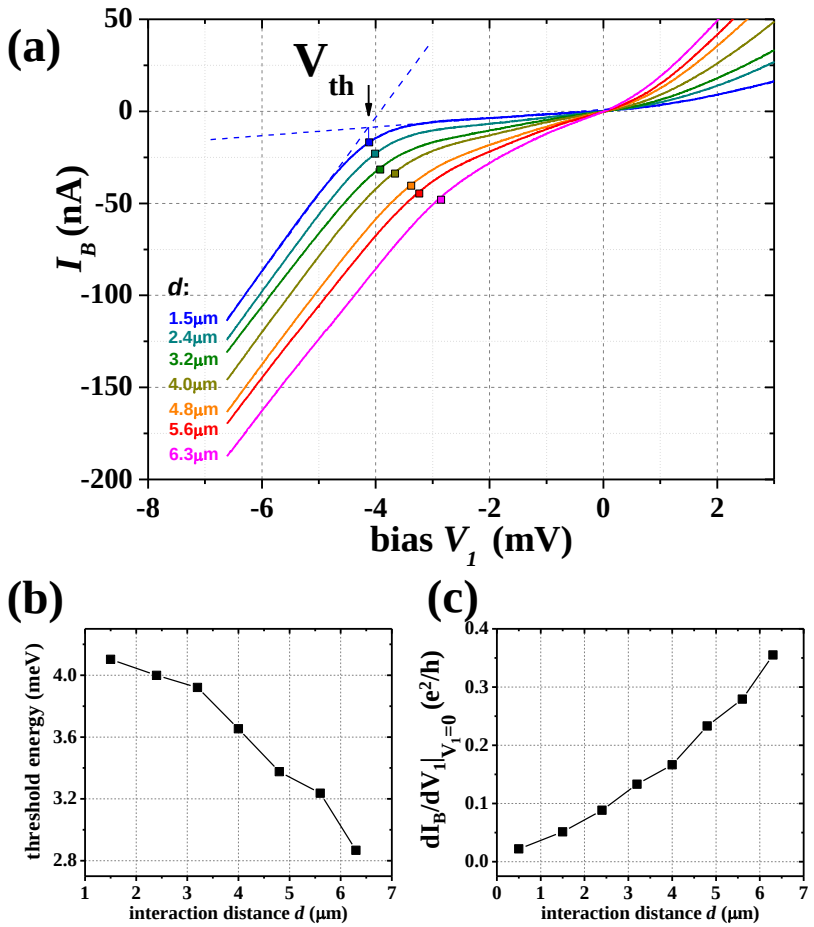

Figure 4.5: (a) Current-voltage characteristics for different values of the junction length d. The threshold points V_{th} (colored dots) have been determined by extrapolating both the zero-bias and the saturation linear behavior (explicitly shown for $d = 1.5$ μm), and taking the intersection point. (b) Threshold energy plotted as a function of d, extracted from the experimentl curves in panel (a). (c) Plot of the zero-bias differential conductance as a function of d.

beyond the threshold, any excess of imbalance between the two edges is perfectly equilibrated.

The most interesting feature in Fig. 4.5(a) concerns the detail of the transition between the two regimes, whose position and shape clearly depends on d. The dependence of the actual threshold voltage $|V_{th}|$ on interaction length is shown in Fig. 4.5(b). It is always smaller than $\hbar\omega_c$ and decreases by increasing d. At the same time, the transition becomes smoother, as shown in Fig. 4.5(a). This is the main finding of this experiment.

The possibility to *track* threshold evolution gives us an important indication about the origin of this phenomenon: in fact, a threshold reduction

accompanied by a smoothening is the typical signature of a temperature increase. Indeed, the experimental evidence discussed in the previous section demonstrates the crucial role of the impurity-induced elastic scattering in equilibrating the edge imbalance. Clearly, for a finite imbalance, such processes inject *hot* electrons in the outer edge. For this reason, we model this process starting from the conservation of the total edge energy, when only the most relevant scattering mechanisms are at work. To discuss our model we shall refer to the scheme shown in Fig. 4.1(a). The two edge channels meet at $x = 0$ with an imbalance $\mu_i(0) - \mu_o(0) = eV_1$. Along the junction length d the imbalance $\Delta\mu(x) \equiv \mu_i(x) - \mu_o(x) \equiv e\Delta V(x)$ will decrease due to scattering events. In this analysis we assume immediate intra-edge relaxation, so that both chemical potential and electron temperature are well defined at each position x. In general, in each junction interval dx the scattered current is given by

$$dI = \Phi(\Delta V(x), T(x))dx, \tag{4.1}$$

where Φ is a function of $\Delta V(x)$ and $T(x)$ depending on the details of the equilibration model (edge dispersion, scattering mechanisms, electron heating etc.). The corresponding changes in the edge potentials are

$$\begin{aligned} V_i(x+dx) &= V_i(x) - \frac{h}{2e^2}dI \\ V_o(x+dx) &= V_o(x) + \frac{h}{2e^2}dI \end{aligned} \tag{4.2}$$

where the factor 2 accounts for the spin degeneracy. From Eqs. 4.1 and 4.2 we obtain:

$$\frac{dI}{dx} = -\frac{e^2}{h}\frac{d}{dx}\Delta V(x) = \Phi(\Delta V(x), T(x)). \tag{4.3}$$

If the temperature dependence of Φ can be neglected, then I_B-V_1 curves can be calculated by solving the Eq. 4.3 for $\Delta V(x)$ with boundary condition $\Delta V(0) = V_1$. The output edge currents are

$$\begin{aligned} I_A &= \frac{2e^2}{h}\frac{V_1 + \Delta V(d)}{2} \\ I_B &= \frac{2e^2}{h}\frac{V_1 - \Delta V(d)}{2}, \end{aligned} \tag{4.4}$$

whose sum equals the total input current $I_{tot} = I_A + I_B = 2(e^2/h)V_1$. If the temperature dependence of Φ cannot be neglected, in order to extract the I_B-V_1 curves it is necessary to define an equation that connects $\Delta V(x)$ and $T(x)$, i.e. a model describing electron heating, as we shall show in the following.

Inter-channel scattering can originate from several processes. At low bias, the inter-edge electron transfer can be either induced by impurity or

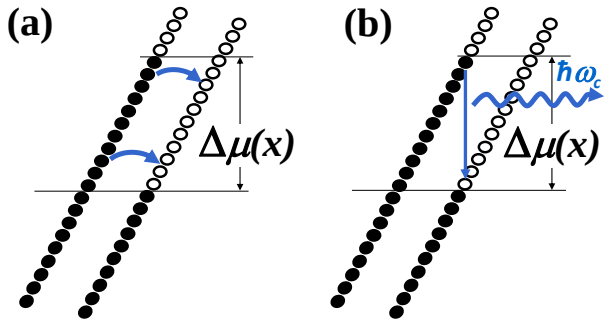

Figure 4.6: (a) Scheme of the impurity-induced elastic scattering for a non-interacting electron system. (b) When the chemical potential of the inner edge becomes higher than the outer one by at least the cyclotron gap $\hbar\omega_c$, vertical radiative transitions can occur. Notice that for opposite polarity vertical transitions are suppressed.

by phonon scattering. [58, 69] The latter, however, was shown to be less important when the base temperature is smaller than 1 K [58, 69]. The dominant process (sketched in Fig. 4.6(a)) is thus elastic scattering induced by the sharp impurity potential which provides the change in momentum needed for inter-channel transition. The scattered current in interval dx is

$$dI = \int_{-\infty}^{\infty} eD(\epsilon)\mathcal{T}(\epsilon)(f_{\mu_i,T}(\epsilon) - f_{\mu_o,T}(\epsilon))d\epsilon, \tag{4.5}$$

where $D(\epsilon)$ is the density of states at energy ϵ and $\mathcal{T}(\epsilon)$ is the elastic scattering probability per unit time.

In order to estimate expressions as the one on the right hand of Eq. 4.5, a model for the edge dispersion is needed. Here we shall assume the simplest case, i.e. a linear dispersion at the edge, that will be justified in the following on the basis of the observed temperature effects. In this approximation, we can approximate both D and $\mathcal{T}$ as constant in the energy window $e\Delta V$. In this case the density of states is $D(\epsilon) = 2dx/(hv_d)$, where v_d is the drift velocity. Thus (see appendix A.2)

$$\begin{aligned} dI &= dx\frac{2e\mathcal{T}_0}{hv_d}\int_{-\infty}^{\infty}(f_{\mu_i,T}(\epsilon) - f_{\mu_o,T}(\epsilon))d\epsilon \\ &= dx\frac{2e^2\mathcal{T}_0}{hv_d}\Delta V(x), \end{aligned} \tag{4.6}$$

where $\mathcal{T}_0$ is the constant transmission probability. For this process Φ is linear in $\Delta V(x)$ and does not depend on T. In this limit, Eq. 4.3 can be easily solved and yields an exponential decay for the edge imbalance

$$\Delta V(x) = V_1 e^{-\frac{2\mathcal{T}_0}{v_d}x}. \tag{4.7}$$

This exponential behavior was assumed in the literature [57, 58, 69] to describe the zero-bias inter-channel scattering in the limit of a uniform distribution of scattering centers. The characteristic length in this case is $\ell_{eq} = v_d/(2\mathcal{T}_0)$, i.e. the average distance between two scattering events. We experimentally verified this exponential decay at the beginning of this chapter [71]. Furthermore, the output current I_B is linear in V_1 (ohmic behavior):

$$I_B = \frac{2e^2}{h}\frac{V_1 - \Delta V(d)}{2} = V_1\frac{2e^2}{h}\frac{1 - e^{-\frac{d}{\ell_{eq}}}}{2}. \tag{4.8}$$

At higher imbalance, comparable to the Landau level gap $\hbar\omega_c$, other equilibration processes become possible. When $\mu_i > \mu_o$ radiative transitions from the inner edge to the outer one are enabled, as depicted in Fig. 4.6(b). Non-vertical relaxation could in principle occur via phonon-assisted transitions. However, this is a second-order effect that can in first approximation be disregarded, at least at low temperatures. The scattered current due to vertical transitions is then given by

$$dI = \int_{-\infty}^{\infty} eD(\epsilon)\mathcal{T}_1(\epsilon)[f_{\mu_i,T}(\epsilon)(1 - f_{\mu_o,T}(\epsilon - \hbar\omega_c))]d\epsilon, \tag{4.9}$$

where $\mathcal{T}_1$ is the probability per unit time for the transition $\epsilon \to \epsilon - \hbar\omega_c$. Since the Landau level bands are parallel, the transition probability is constant in energy. Therefore we can simplify Eq. 4.9

$$\begin{aligned} dI &= dx\frac{2e\mathcal{T}_1}{hv_d}\int_{-\infty}^{\infty}[f_{\mu_i,T}(\epsilon)(1 - f_{\mu_o,T}(\epsilon - \hbar\omega_c))]d\epsilon \\ &= dx\frac{2e\mathcal{T}_1}{hv_d}\left(\frac{e\Delta V(x) - \hbar\omega_c}{1 - e^{\frac{\hbar\omega_c - e\Delta V(x)}{k_B T}}}\right) \end{aligned} \tag{4.10}$$

where the integration is explicitly shown in appendix A.2. In the Φ function we also have a non-linear addendum, thus the integration of Eq. 4.3 must be performed numerically. At low temperature, due to the exponential term, the effect of the term in Eq. 4.10 is negligible for $\Delta V(x)$ below the threshold $\hbar\omega_c$. For $\Delta V(x) > \hbar\omega_c$ the availability of empty states in the lower Landau level gives rise to radiative relaxation. As shown in recent experiments [68], the photons emitted in this process can indeed be collected with a suitable waveguide and detected.

So far we completely neglected the effect of the electron heating due to the injection of hot carriers. In order to obtain a quantitative estimate of the amount of energy transferred to the electron system, we need to first estimate the total energy increase for an edge channel when we increase its chemical potential from the ground level $\mu = \mu_0$ to an arbitrary level $\mu = \mu_j$ and its temperature from $T = 0$ to $T = T_j$

$$\mathcal{E}_j = \int_{-\infty}^{\infty}\frac{2d}{hv_d}(\epsilon - \mu_0)(f_{\mu_j,T}(\epsilon) - f_{\mu_0,0}(\epsilon))d\epsilon$$

$$\approx \frac{1}{2}\frac{2\tau}{h}(\mu_j - \mu_0)^2 + \frac{2\tau}{h}\frac{\pi^2}{6}k_B^2 T_j^2, \tag{4.11}$$

where in the second line we approximated the integral with its first order Sommerfeld expansion (as shown in detail in appendix A.3) and $\tau \equiv d/v_d$.

In order to calculate explicitly the output temperature $T(x)$ we shall assume energy conservation in each element dx

$$\mathcal{E}_i(x) + \mathcal{E}_o(x) = \mathcal{E}_i(x+dx) + \mathcal{E}_o(x+dx), \tag{4.12}$$

together with three additional approximations: (i) the two edges immediately restore the thermal equilibrium after each scattering event; (ii) the temperature is approximately the same in both edges $T_i(x) = T_o(x) = T(x)$, with $T(0) = T_{in}$, where T_{in} is the bulk electron temperature; (iii) in each element dx only the ohmic part of the scattered current dI contributes to electron heating. In fact, while elastic processes transfer hot carriers between the two edges, radiative terms allow electrons to relax by photon emission. With these assumptions, after substituting Eq. 4.11 into Eq. 4.12 (as seen in Appendix A.4), we have an expression linking the change in temperature to the local imbalance

$$\frac{d}{dx}T(x) = \frac{3e^2}{4\pi^2 k_B^2 \ell_{eq}}\frac{\Delta V^2(x)}{T(x)}. \tag{4.13}$$

Equation 4.3 must be solved together with Eq. 4.13 to obtain both $T(x)$ and $V(x)$. Due to electron heating, the onset of radiative transitions is shifted below the cyclotron gap value $\hbar\omega_c$ since thermally-excited electrons leave available states in a range of about $k_B T$ around the chemical potential of the lower level. The transition itself becomes smoother, since the expression in Eq. 4.10 is less steep at higher temperatures.

Figure 4.7(a) shows the I_B-V_1 characteristics (red dots) at low bias for the $d = 2.4$ μm case. The behavior is clearly ohmic, as confirmed by a

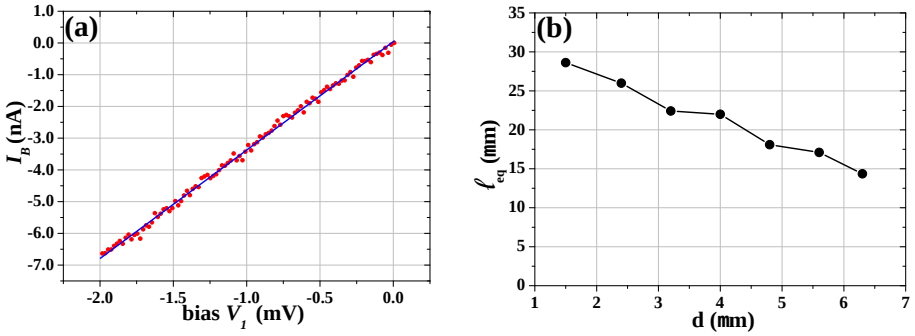

Figure 4.7: (a) Detail of the I_B-V_1 characteristics in the range -2 mV$< V_1 <$ 0, for $d = 2.4$ μm (red dots). The behavior is ohmic as evidenced by the linear fit (blue line). (b) Plot of ℓ_{eq} for different junction lengths d.

linear fit (blue line, adjusted $R^2 = 0.997$). This agrees with the predictions of our model at low bias, when radiative emission is negligible and Eq. 4.8 applies. The zero-bias differential conductance depends on the distribution of scattering centers inside the constriction. Equation 4.8 allows us to obtain the equilibration length ℓ_{eq} by fitting the I_B-V_1 curves in the linear region. Figure 4.7(b) displays the different ℓ_{eq} values obtained for each junction length d. The average ℓ_{eq} value (21 μm) is compatible with the one reported in section 4.1 (15 μm), considering that those results were obtained from different samples. The graph evidences that ℓ_{eq} depends on d. As shown in section 4.1, the actual impurity density is highly sample-dependent and can fluctuate along inter-channel junction. The monotonic decrease observed in Fig. 4.7(b) could however indicate that for small d values scattering centers are somewhat less effective, due to the fact that the edges are smoothly brought into interaction and separated. Therefore the inter-channel separation is larger at the constriction entrance than at the inner points. These boundary effects are more important for smaller d.

The previous results provide the first of the two free parameters in our model, namely ℓ_{eq} and $\mathcal{T}_1$. Therefore we fit the experimental curves in Fig. 4.5 with the functions obtained solving Eqs. 4.3 and 4.13, with the only fitting parameter $\mathcal{T}_1$. The fit for $d = 2.4$ μm is displayed in Fig. 4.8(a), together with the experimental data. The agreement between the two curves is remarkable: our simple model reproduces well the main features observed in Fig. 4.5. The threshold shift can be better seen in Fig. 4.8(b), where we plot the fitting curves for the same d values in Fig. 4.5. In the inset we show a comparison between the threshold voltage values extracted from the fitting curves and the ones directly estimated from the I_B-V_1 characteristics. This graph indicates that the present model successfully describes the observed threshold reduction. The value for the Landau level gap ($\hbar\omega_c = 5.74$ meV) was kept constant in these fits. This value turns out to be optimal once both ℓ_{eq} and $\mathcal{T}_1$ have been determined, in fact any further adjustment of the gap decreases the fit quality.

This result explains the reduction of the threshold for photon emission observed in several experiments [60, 68]. The significant deviation from $\hbar\omega_c/e$ is an effect due to electron heating induced by the injection of hot carriers in the outer edge via elastic scattering.

In order to quantitatively estimate the electron temperature increase, we solved Eq. 4.13, using the parameters ℓ_{eq} and $\mathcal{T}_1$ provided by the previous fits, with the initial condition $T_{in} = 400$ mK. Figure 4.9 shows the solutions for the d values corresponding to the experimental data in Fig. 4.5. For small bias the temperature increases almost quadratically with the imbalance, while for intermediate values the behavior is approximately linear, with a slope proportional to d. Finally, temperature tends to saturate at the onset of radiative emission, which suppresses further injection of hot electrons into the outer edge. At saturation, the output edge temperatures are by far

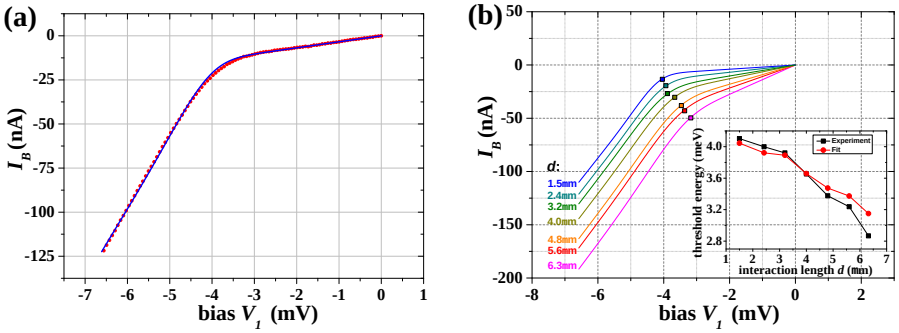

Figure 4.8: (a) Fit (blue line) of the I_B-V_1 curve for $d = 2.4$ μm (red dots) using solutions of Eqs. 4.3 and 4.13, with the parameter ℓ_{eq} obtained from the previous linear fits. (b) The corresponding fitting curves of the experimental data shown in Fig. 4.5. (inset) Threshold voltages plotted as a function of d as deduced from the fitting curves (red dots), together with the values directly extracted from Fig. 4.5 (black squares).

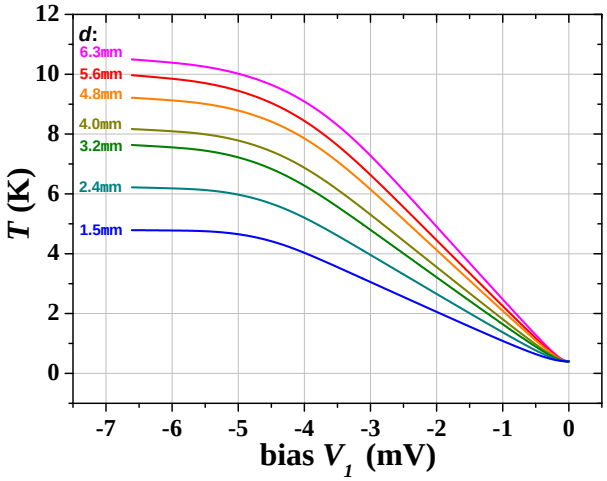

Figure 4.9: Bias dependence of the outgoing electron temperature plotted for different d values. The curves are obtained from Eq. 4.13, with the initial condition $T(0) = 400$ mK. The parameters ℓ_{eq} and $\mathcal{T}_1$ are obtained from the previous fits of the experimental data.

larger than the base temperature.

So far we have considered a linear edge dispersion, which neglects effects of edge reconstruction due to electron-electron interactions [10]. We have also developed alternative models, that take into account the effect of the compressible and incompressible stripes at the sample edge. While such more complex analysis correctly predicts the linear behavior at low bias, it is less satisfactory in describing the threshold evolution, although it contains more adjustable parameters (e.g. the compressible and incompressible stripe

widths). We interpreted such a discrepancy as the effect of the high electron temperature induced by the elastic scattering processes and present on most part of the edge junction.

Chapter 5

Conclusion

The edge picture is a paradigmatic example of a good scientific *model*. Although simple, it yields precise and well-defined predictions, and successfully explained and unified a number of experimental findings. For a long time, however, nobody could directly observe edge states. Maps of the edge channels became available only with the advent of SPM techniques. As discussed in chapter 2, early spatially-resolved measurements were rather motivated by the need to verify the *limits* of the edge picture itself, namely the effect of electron-electron interactions on the edge structure, as described in chapter 1. SPM allowed to electrostatically detect the charge pile-up at the sample edge and image channel trajectories. Unfortunately spatial resolution was not sufficient to reveal the edge structure.

This thesis provides *the first image of the inner fractional structure* of individual integer edge channels: SGM maps show that it consists of a series of alternating compressible and incompressible stripes. The latter are observed when the local filling factor corresponds to a robust fraction. The high spatial resolution achievable with our technique allowed us to quantitatively test the predictions of the reconstruction theory [10]. The experimental results presented in section 3.4 demonstrate that both the measured incompressible stripe widths and their dependence on electron density profiles are in excellent agreement with the model introduced by Chklovskii [10, 72]. The experimental demonstration of fractional structures within integer edge channels represents the conclusive answer to long-time debated issues. The stripe structure explains how edge channels behave at the interface between an integer and a fractional QH phase. In this case, an integer edge is partitioned into its fractional components, so that there is continuity between the fractional incompressible stripe and the corresponding macroscopic fractional phase. This also elucidates the non-fermionic characteristics observed by finite bias measurements on point-like junctions between *integer* QH phases [27].

In our experiments we also demonstrated how to accurately control edge-

channel trajectories. This ability introduces a new degree of freedom in transport measurements: the *device geometry* itself can become a tunable experimental parameter, controllable in real time at low temperature, exactly as the gate bias, the injected current, or the applied magnetic field. The unprecedented flexibility of this method opens the way to a number of experimental opportunities, such as the one discussed in chapter 4: we used a size-tunable QH circuit to image the effect of the disorder-induced potential modulations to charge equilibration between co-propagating edge channels. These measurements clarified important findings of previous transport experiments: on one hand our data unambiguously showed the link between inter-edge scattering and the presence of potential fluctuations. On the other hand, they allowed to explain the puzzling reduction of the threshold voltage for the onset of radiative emission [60, 66, 68] .

We believe that this ability to explain and clarify fundamental (and debated) issues of QH physics makes these results relevant by themselves. The main motivation for our research, however, is related to the possibility to implement a beam mixer for co-propagating edge channels, the critical element of a new class of quantum electron interferometers, as described in section 1.4. In our laboratory, two different strategies to implement such a challenging device are under study, depending on the type of edge channels to be mixed. In case of two spin-split edge channels (fully spin polarized), there is a good overlap between the orbital component of the wavefunctions, whereas the spin components are completely orthogonal. A possible strategy consists in applying a perturbative in-plane magnetic field, which allows to precess the spins, and thus to induce a coherent mixing [73]. On the other hand, if the edge channels to be mixed are spin degenerate, disorder-induced fluctuations are sufficient to generate inter-edge scattering, as we showed in chapter 4. However, other processes were invoked in the literature to explain this mixing, e.g. acoustic phonon scattering [58]. Such additional processes, if relevant, would destroy the phase coherence. For this reason, the results reported in section 4.1 are crucial to determine if potential modulations can be employed to achieve a coherent beam mixer. Our data indicate that the dominant equilibration process is impurity-induced scattering. This suggests that a coherent beam mixing should be possible. However, in order to demonstrate that coherence is preserved, a specific interferometric test is required.

Figure 5.1 shows our proposal for such a device. It is a development of the QH circuit depicted in Fig. 4.1. A selector gate (g_2) allows to imbalance two edge channels that come from distinct source contacts **1a** and **1b**. The channels meet at the entrance of a long constriction, where they are mixed. The inner edge is reflected by the tip, while the outer one is reflected by a shutter gate (g_3). The two edge channels thus meet again after having accumulated an Aharonov-Bohm phase difference Φ proportional to the magnetic flux piercing the area between the two alternative paths (see Fig. 5.1). Next,

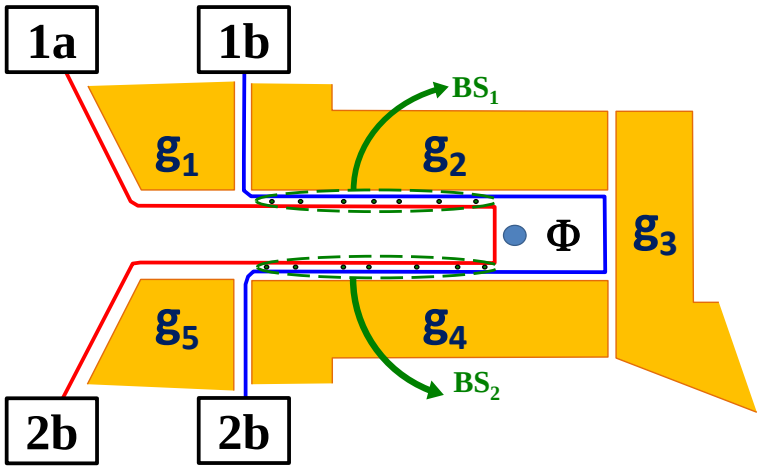

Figure 5.1: The device discussed in chapter 4 can be used as a simply-connected MZI by using a shutter gate ($\mathbf{g_3}$) and an additional selector gate ($\mathbf{g_5}$). The two interacting channels are mixed again on the bottom edge of the constriction, after having accumulated an Aharonov-Bohm phase difference Φ. Then, they are separated and sent to two detecting contacts (**2a** and **2b**). Notice that the edge channel topology is the same as the one in Fig. 1.6.

the bottom part of the constriction acts as second beam splitter (as $\mathbf{BS}_2$ in the scheme of Fig. 1.6). The two outgoing edges are separated and sent to two different contacts using another selector gate (g_5 in the scheme). Topologically, this QH circuit is the same as the one proposed by Giovannetti *et al.* [9]. In this case, the magnetic flux (and thus the Aharonov-Bohm phase) can be changed (i) by moving the tip, or (ii) by lateral depletion using the gate g_3, or (iii) by changing the magnetic field. Preliminary experiments on one such device were actually already performed. The results we obtained so far are not conclusive.[1] The main difficulty is related to the compromise between the need to have a suitable inter-channel mixing (which requires an interaction path length d of a few microns) with the constraint that the total length of the device (the two beam splitters plus the interference path) is less than the coherence length ℓ_ϕ, which scales as T^{-1} [74]. The values reported for ℓ_ϕ at 20 mK range from 20 μm [6, 74] to 80 μm [75]. Therefore, the expected value at 400 mK (the electron temperature available in our setup) is 1–4 μm, which reduces the possible length of the beam mixer to 0.5–2 μm: as we have shown in chapter 4, within such distances it is difficult to obtain a good mixing via random impurities. Near-future developments of our work are related to the possibility to perform measurements at lower temperatures (i.e. in a dilution-fridge SGM). A decrease of the electron tem-

[1] A few weak oscillations in the transmitted signal were actually observed. Their periodicity however does not allow us to correlate the oscillations to the geometry of the interfering paths.

perature may make ℓ_ϕ large enough to achieve good mixing without losing electron phase coherence, since the ℓ_ϕ values reported at 20 mK are much larger than the length required to obtain a good mixing by means of random impurities. Another possible strategy consists in *inducing* strong scattering centers in a controllable manner, e.g. by inducing surface charge accumulation by means of an AFM tip. In this way we can obtain good inter-channel mixing even for short (< 1 μm) interferometers.

As shown in chapter 3, our experimental conditions allow to observe a complex inner-edge structure. In the Introduction, we argued that the fractional components that form the edge channels can be used as building blocks for interferometers working with anyons instead of fermions. The possibility to use fractional stripes as independent channels depends on the robustness of the incompressible stripes that separate the imbalanced compressible stripes. As discussed in section 3.4, in the fractional QH regime the quasi-particle gaps (and thus the incompressible stripe width) depend on both temperature and disorder [55]. For this reason, the SGM measurements on QPCs would benefit from an increase of the 2DEG mobility ($\mu > 10^7$ cm^2/Vs) and a decrease of the electron temperature. This would allow to operate the interferometer shown in Fig. 5.1 with individual *fractional* stripes instead of single integer edge channels.

The impact of such a result should not be underestimated since it would represent a valid step forward towards the achievement of an interferometer operating with exotic quasi-particles, like the non-abelian excitations of the $\nu = 5/2$ QH phase. Such an advance would in perspective lead to the implementation of unprecedentedly fault-tolerant quantum computers, because of the nonlocal encoding of the quasiparticle states, which makes them immune to errors caused by local perturbations [76].

Appendix A

Quantum Hall calculations

A.1 Landau quantization

The single-particle Hamiltonian describing the physics of one electron confined in two dimensions, in the presence of a strong magnetic field $\mathbf{B} = B\hat{z}$, is:

$$\mathcal{H} = \frac{(\mathbf{p} + e\mathbf{A})^2}{2m^*} = \frac{p_x^2}{2m^*} + \frac{(p_y + eBx)^2}{2m^*}, \tag{A.1}$$

where we used the Landau gauge $\mathbf{A} = xB\hat{y}$, which is particularly convenient for translationally invariant systems, as an infinitely long Hall bar. The translation symmetry in the $\hat{y}$ direction allows us to write the wavefunction as an eigenstate of p_y

$$\psi_k(x, y) = e^{iky}\varphi_k(x), \tag{A.2}$$

where we replaced $p_y \to \hbar k$. After separating variables, we have

$$\mathcal{H}'_k\varphi_k(x) = \varepsilon_k\varphi_k(x), \tag{A.3}$$

where

$$\mathcal{H}'_k = \frac{p_x^2}{2m^*} + \frac{(\hbar k + eBx)^2}{2m^*} = \frac{p_x^2}{2m^*} + \frac{1}{2}m^*\omega_c^2(x + k\ell_B^2)^2. \tag{A.4}$$

The term $\mathcal{H}'_k$ in Eq. A.4 describes a displaced 1D harmonic oscillator, whose center coordinate $X_k \equiv -k\ell_B^2$ is proportional to the momentum quantum number along $\hat{y}$. The energy spectrum is thus

$$\varepsilon_{nk} = \left(n + \frac{1}{2}\right)\hbar\omega_c, \tag{A.5}$$

where $\omega_c = eB/m^*$ is the cyclotron frequency. The eigenfunctions are

$$\psi_{nk}(x, y) \propto e^{iky}H_n(x + k\ell_B^2)e^{-(x+k\ell_B^2)^2/2\ell_B^2}, \tag{A.6}$$

where H_n is the n-th Hermite polynomial.

In order to include the spin, we must add the Zeeman term $\mathcal{S}_z g^* \mu_B B$ to the Hamiltonian $\mathcal{H}$. As a consequence, each orbital level is split[1] into two levels (the so-called *Landau levels*) with well defined spin orientation.

Since the single-particle energies do not depend on the momentum along $\hat{y}$, the Landau levels are extremely degenerate. In order to calculate the degeneracy, let us consider a rectangular Hall bar with dimensions $L_x \times L_y$, whose extremes in x are $x_{min} = -L_x$ and $x_{max} = 0$. The basis states which are confined within the bar have the wavevector k that ranges from $k = 0$ to $k = L_x/\ell_B^2$. The total number of states in each Landau level is thus

$$N = \int_0^{L_x/\ell_B^2} \left(\frac{L_y}{2\pi}\right) dk = \frac{L_x L_y}{2\pi\ell_B^2}, \tag{A.7}$$

so that the degeneracy per unit area is $n_L = (2\pi\ell_B^2)^{-1}$ (Eq. 1.1).

In any real sample there is an external potential $U(x)$ which confines electrons within the Hall bar. If $U(x)$ is slowly varying on the magnetic length scale, it will only couple basis states that have almost the same center coordinate X_k. Although the φ_k are no longer the eigenfunctions of the harmonic oscillator, they will be nonetheless still peaked near $X_k = -k\ell_B^2$. The first-order correction to the single-particle energies is thus

$$\langle \psi_{nk} \mid U(x) \mid \psi_{nk} \rangle \approx U(-k\ell_B^2). \tag{A.8}$$

The confinement potential gives therefore an additional term which produces a band-bending at the sample edge depicted in Fig. 1.2. The group velocity

$$v_k = \frac{1}{\hbar}\frac{\partial \varepsilon_k}{\partial k} \approx -\frac{\ell_B^2}{\hbar}\left.\frac{dU}{dx}\right|_{X_k} \tag{A.9}$$

is opposite on the two edges of the sample (counter-propagating edges). The expression for the group velocity allows us to calculate the fundamental relation between Hall voltage and net current transmitted in a Hall bar (Eq. 1.3). As discussed in section 1.1, due to the chirality and to the suppression of backscattering, the counter-propagating edge channels can be in equilibrium with two distinct and imbalanced contacts, and thus they can have different chemical potentials. For each Landau level, the total current is given by

$$I_0 = -\frac{e}{L_y}\int_{-\infty}^{+\infty} \frac{L_y}{2\pi}\frac{1}{\hbar}\frac{\partial \varepsilon_k}{\partial k} f_0(k) dk, \tag{A.10}$$

where f_0 is the occupation probability for the k state in the Landau level. At $T = 0$ the integral can be easily evaluated

$$I_0 = -\frac{e}{L_y}\int_{-\mu_R}^{\mu_L} d\varepsilon = \frac{e}{h}(\mu_R - \mu_L) \equiv \frac{e^2}{h} V_0, \tag{A.11}$$

[1] In GaAs ($g^* = -0.44$) the Zeeman splitting $\hbar\omega_c$ is about 70 times smaller than the cyclotron splitting.

where μ_L and μ_R are the chemical potential of the left and right contact, respectively. Notice that if ν different Landau levels are occupied, we recover Eq. 1.3.

A.2 Integration of expressions containing Fermi functions

In Eq. 4.6 we evaluated the integral

$$\int_{-\infty}^{\infty}(f_{\mu_i,T}(\epsilon)-f_{\mu_o,T}(\epsilon))d\epsilon = \\ =\int_{-\infty}^{\infty}\left(\frac{1}{1+e^{\frac{\epsilon-\mu_i}{k_BT}}}-\frac{1}{1+e^{\frac{\epsilon-\mu_o}{k_BT}}}\right)d\epsilon. \tag{A.12}$$

Defining $x\equiv\epsilon/k_BT$, $x_i\equiv\mu_i/k_BT$ and $x_o\equiv\mu_o/k_BT$, we have

$$\int_{-\infty}^{\infty}\left(\frac{1}{1+e^{x-x_i}}-\frac{1}{1+e^{x-x_o}}\right)k_BTdx. \tag{A.13}$$

A primitive of the expression in brackets is

$$-\ln(1+e^{x-x_i})+\ln(1+e^{x-x_o}), \tag{A.14}$$

thus

$$\begin{aligned}&\int_{-\infty}^{\infty}\left(\frac{1}{1+e^{x-x_i}}-\frac{1}{1+e^{x-x_o}}\right)k_BTdx = \\ =\ &\lim_{x\to+\infty}k_BT\left[-\ln(1+e^{x-x_i})+\ln(1+e^{x-x_o})\right]+ \\ -\ &\lim_{x\to-\infty}k_BT\left[-\ln(1+e^{x-x_i})+\ln(1+e^{x-x_o})\right]= \\ =\ &k_BT(x_i-x_o)-0=\mu_i-\mu_o=e\Delta V.\end{aligned} \tag{A.15}$$

In Eq. 4.10 we evaluated the integral

$$\int_{-\infty}^{\infty}[f_{\mu_i,T}(\epsilon)(1-f_{\mu_o,T}(\epsilon-\hbar\omega_c))]d\epsilon. \tag{A.16}$$

Defining $x\equiv\epsilon/k_BT$, $x_i\equiv\mu_i/k_BT$ and $x_o\equiv(\hbar\omega_c+\mu_o)/k_BT$, we have

$$\int_{-\infty}^{\infty}\left[\frac{1}{1+e^{x-x_i}}\left(1-\frac{1}{1+e^{x-x_o}}\right)\right]k_BTdx. \tag{A.17}$$

A primitive of the expression in square brackets is

$$\frac{e^{x_i}}{e^{x_i}-e^{x_o}}\ln\left(\frac{e^{x_o}+e^{x}}{e^{x_i}+e^{x}}\right), \tag{A.18}$$

thus

$$\begin{aligned}
&\int_{-\infty}^{\infty}\left[\frac{1}{1+e^{x-x_i}}\left(1-\frac{1}{1+e^{x-x_o}}\right)\right]k_BTdx = \\
= &\lim_{x\to+\infty} k_BT\left[\frac{e^{x_i}}{e^{x_i}-e^{x_o}}\ln\left(\frac{e^{x_o}+e^{x}}{e^{x_i}+e^{x}}\right)\right] + \\
- &\lim_{x\to-\infty} k_BT\left[\frac{e^{x_i}}{e^{x_i}-e^{x_o}}\ln\left(\frac{e^{x_o}+e^{x}}{e^{x_i}+e^{x}}\right)\right] = \\
= &\; k_BT\left[0-\frac{e^{x_i}}{e^{x_i}-e^{x_o}}(x_o-x_i)\right] = \\
= &\; k_BT\frac{x_i-x_o}{1-e^{x_o-x_i}} = \frac{e\Delta V-\hbar\omega_c}{1-e^{\frac{\hbar\omega_c-e\Delta V}{k_BT}}}.
\end{aligned} \tag{A.19}$$

A.3 First order approximation to the edge energy

In order to evaluate the first line of Eq. 4.11 we exploit the Sommerfeld expansion

$$\begin{aligned}
&\int_{-\infty}^{\infty}\frac{g(\epsilon)}{1+e^{\frac{\epsilon-\mu}{k_BT}}}d\epsilon = \\
= &\int_{-\infty}^{\mu} g(\epsilon)d\epsilon + \frac{\pi^2}{6}k_B^2T^2g'(\mu) + O\left(\frac{k_BT}{\mu}\right)^4
\end{aligned} \tag{A.20}$$

where $g(\epsilon)$ is a generic function of ϵ and $g'(\mu)$ is its first derivative evaluated at $\epsilon=\mu$. By applying this relation to Eq. 4.11 we obtain

$$\begin{aligned}
&\int_{-\infty}^{\infty}\frac{2d}{hv_d}\frac{\epsilon-\mu_0}{1+e^{\frac{\epsilon-\mu}{k_BT}}}d\epsilon - \int_{-\infty}^{\mu_0}\frac{2d}{hv_d}(\epsilon-\mu_0)d\epsilon \approx \\
\approx &\int_{\mu_0}^{\mu_j}\frac{2d}{hv_d}(\epsilon-\mu_0)d\epsilon + \frac{2d}{hv_d}\frac{\pi^2}{6}k_B^2T_j^2 = \\
= &\; \frac{1}{2}\left(\frac{2\tau}{h}\right)(\mu_j-\mu_0)^2 + \left(\frac{2\tau}{h}\right)\frac{\pi^2}{6}k_B^2T_j^2.
\end{aligned} \tag{A.21}$$

A.4 Determination of $T(x)$

When the electron temperature is non-zero, the expression for the total edge energy has an extra term proportional to T^2, as seen in Eq. A.21. We can thus define the electrostatic and the thermal component of the total edge energy:

$$\begin{aligned}
E^{el} &\equiv \frac{1}{2}\left(\frac{2\tau}{h}\right)(\mu_j-\mu_0)^2 = \frac{1}{2}\left(\frac{2\tau}{h}\right)e^2V_j^2 \\
E^{th} &\equiv \left(\frac{2\tau}{h}\right)\frac{\pi^2}{6}k_B^2T_j^2
\end{aligned} \tag{A.22}$$

where V_j is the edge voltage referred to the ground. Equation A.22 allows us to evaluate Eq. 4.12. As discussed in chapter 4, only elastic scattering processes transfer hot carriers between the edges, while the radiative term allows electrons to relax by photon emission. Thus we modify Eqs. 4.2 as follows

$$\begin{aligned} V_i(x+dx) &= V_i(x) - \frac{h}{2e^2} dI^{elast.} \\ &= V_i(x) - \frac{h}{2e^2}\frac{e^2}{h}\frac{1}{\ell_{eq}}\Delta V(x)dx \\ V_o(x+dx) &= V_o(x) + \frac{h}{2e^2} dI^{elast.} \\ &= V_o(x) + \frac{h}{2e^2}\frac{e^2}{h}\frac{1}{\ell_{eq}}\Delta V(x)dx. \end{aligned} \tag{A.23}$$

After evaluating Eq. 4.12 with Eq. A.22, using the substitutions A.23 we obtain

$$\frac{2\pi^2}{3} k_B^2 T(x) dT = \frac{e^2}{2}\frac{1}{\ell_{eq}}\Delta V^2(x)dx \tag{A.24}$$

(where $T_i(x) = T_o(x) = T(x)$) from which Eq. 4.13 easily follows.

Appendix B

Analysis of the SGM maps

B.1 SGM maps and the reconstruction picture

In order to correlate our experimental data (SGM maps of Fig. 3.8) with the reconstruction picture [10, 72], it is useful to start with the well-established [46, 77] single-particle case. We shall first discuss integer channels at the edge of QH systems with bulk filling factor $\nu_b = 2$. Figure B.1(a) shows the single-particle energy dispersion within the QPC for the case of full transmission ($G_T = \nu_b G_0 = 2G_0$) [77]. The energy dispersion is self-consistently determined by gate potentials (split-gates plus the SGM tip) and electron screening. The latter depends on the local compressibility, which is in turn determined by the local electron density. When the two counter-propagating channels are separated by an incompressible phase at the QPC center, backscattering is prevented by Pauli principle: all single-particle states within the incompressible stripe are populated, therefore backscattering can only occur via electron tunneling from a compressible stripe to the counter-propagating one. Due to the presence of the incompressible stripe, the distance between the compressible stripes is larger than the magnetic length, so that the probability for tunneling events is highly suppressed. The detailed shape of the confining potential is influenced by QPC polarization and by tip positioned bias. In particular the distance between compressible stripes,can be reduced by moving the tip towards the QPC center. As shown in Fig. B.1(b), the two counter-propagating stripes can be forced to merge at the QPC center: backscattering is thus enabled ($G_0 < G_T < 2G_0$). When the QPC width is further reduced, an incompressible phase is induced at the QPC center (now with filling factor $\nu = 1$, as shown in Fig. B.1(c)). In this configuration the transmitted conductance is $G_T = G_0$, since one edge is completely reflected. Note that further backscattering can only be induced if we merge the two external compressible stripes. As a consequence, a plateau is observed in the SGM map: a tip displacement does not increase backscattering, unless it is large enough to merge the two remaining compressible

stripes. For this reason, the plateau width is in good approximation twice the incompressible stripe width [46].

In the bottom part of Fig. B.1, we report the electron density profile for each configuration (a–c). When the electron phase is locally gapped (incompressible stripes), the electron density is constant and equals a multiple of the LL degeneracy n_L. Vice versa, when the electron screening is effective, the energy dispersion is flat, and the density changes.

The same picture can be applied to a single integer edge in a $\nu_b = 1$ QH system. At the sample edge, the electron density monotonically decreases. When the local filling factor equals a robust fraction, a fractional incompressible phase is established, due to the condensation of fractional quasi-particles. Within this stripe, electron density is constant. When an incompressible phase is induced at the QPC center, it isolates the adjacent compressible stripes, so that a plateau in the G_T signal is observed. The behavior of fractional and integer stripes is thus very similar: the SGM-map features depend only on the local electron compressibility.

Figure B.2 shows a sketch of the reconstruction picture for the fractional compressible and incompressible stripe distribution within a QPC in a QH

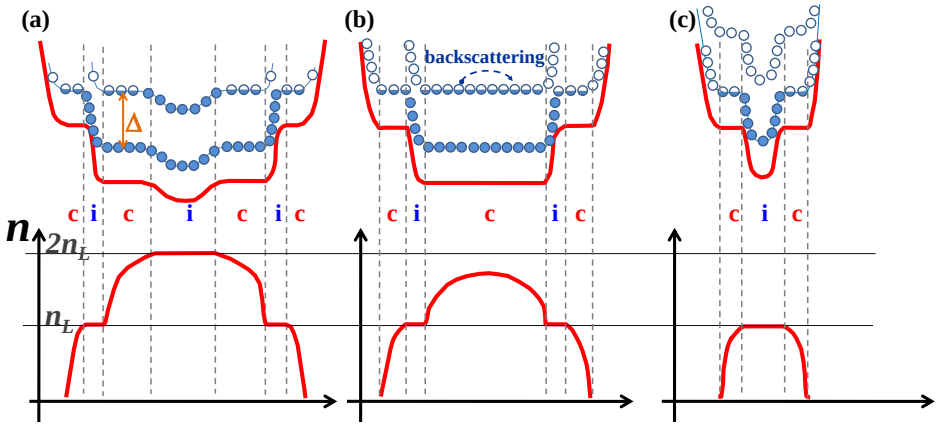

Figure B.1: (a) Top panel: schematic picture of single-particle energy dispersion within a QPC in a QH system at bulk filling factor $\nu_b = 2$, in the case of full transmission ($G_T = 2G_0$) [77]. The width of compressible (c) and incompressible (i) stripes depends on both the local electron density and the energy gap Δ between the LLs. In this case the QPC width is large enough to allow full transmission ($G_T = 2G_0$). Bottom panel: the corresponding electron density function. (b) When the QPC is shrunk, two counter-propagating compressible stripes merge at the QPC center, so that backscattering is enabled. (c) A further decrease of the QPC width induces an incompressible phase with filling factor $\nu = 1$ at the QPC center. At this point, to induce further backscattering it is necessary to merge the remaining compressible stripes. This requires to shrink the QPC width by an amount $2\delta_{IS}$, where δ_{IS} is the incompressible stripe width.

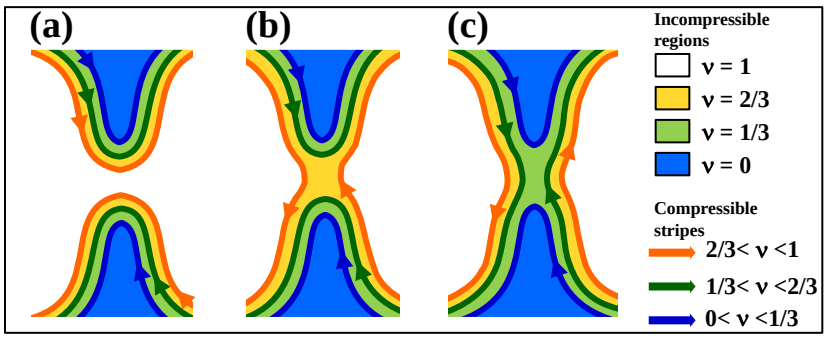

Figure B.2: (a) Scheme of the compressible and incompressible stripe configuration in a QPC, in the case of full transmission. The bulk filling factor is $\nu_b = 1$, hence $G_T = G_0$. For simplicity, in the sketch we only considered the $\nu = 1/3$ and $\nu = 2/3$ fractions. (b) Stripe configuration when the filling factor at the QPC center is $\nu = 2/3$ (incompressible phase). In this case, one third of the current is reflected, so that $G_T = 2/3G_0$. (c) Stripe configuration corresponding to $G_T = 1/3G_0$. See also Fig. 2 of Ref. [28].

system at $\nu_b = 1$. The three panels (a–c) show how the stripe configuration changes when the QPC is gradually pinched off. Panel (a) shows the case of full transmission. In this case, an integer incompressible stripe at filling factor $\nu_{IS} = \nu_b = 1$ separates the two counter-propagating edges, exactly as in Fig. B.1(c). The transmitted conductance does not decrease until we merge the counter-propagating stripes: then it monotonically decreases until a fractional incompressible stripe (at $\nu_{IS} = 2/3$ and $\nu_{IS} = 1/3$ in Fig. B.2(b) and B.2(c), respectively) is induced at the QPC center. At this point, small changes in the QPC width do not change the backscattered current, exactly as observed in the integer case (Fig. B.1(c)). In correspondence to the plateaus, the transmitted current is thus $G_T = \nu_{IS} G_0$.

B.2 Estimate of δ_{IS} from the SGM maps

As discussed in the section 3.3, signatures of the fractional incompressible stripes can be emphasized by counting the occurrences of all the G_T values in the SGM map, and reporting them in a histogram. Plateaus in the SGM maps are displayed as peaks in the histogram in correspondance to $G_T = \nu G_0$, where ν is a robust fraction. Figure B.3(a) shows the histograms corresponding to 9 SGM scans performed on the same area as in Fig. 3.8. All fractional peaks are clearly visible in each individual histogram[1]. Spurious

[1]Provided that the G_T value corresponding to the peak lies within the range of G_T values occurring in the scan. For example, for $V_{tip} = -7.5$ V, the transmitted conductance in the area of interest is never higher than 0.63 e^2/h, thus the 2/3 peak is not visible in this scan. On the contrary, for $V_{tip} = -3.5$ V the conductance in the same area is always

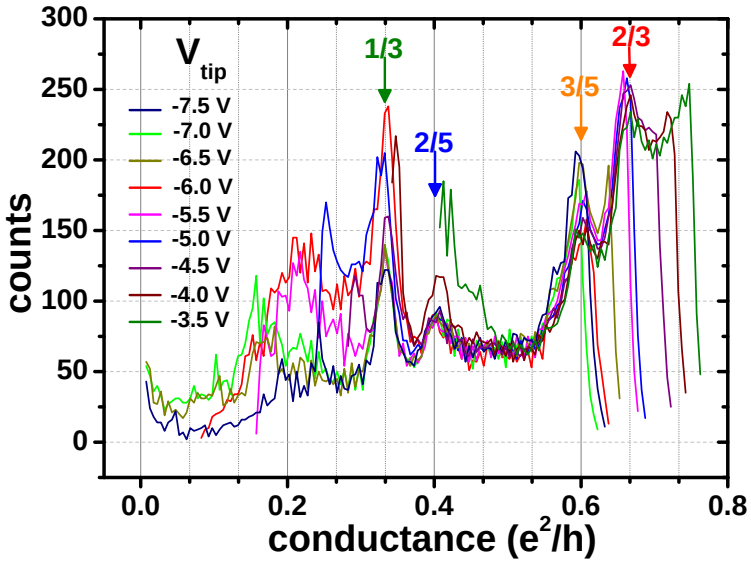

Figure B.3: Histograms of the occurrence of each G_T value for all the 9 different SGM scans performed at different V_{tip} values. Fractional peaks are visible in each individual histogram.

structures are still visible in some scans, but they are removed by averaging all scans. The resulting averaged histogram was reported in Fig. 3.9, which is plotted here in Fig. B.3 for convenience. All histograms in Fig. B.3 terminate with an abrupt decrease of G_T occurrence, which corresponds to the cut-off determined by the scan area. The highest G_T values lie outside the scan area, thus their occurrences are suddenly suppressed. These steep thresholds are responsible of the noisy structures at high conductance values in the averaged curve of Fig. 3.9.

The incompressible stripe width δ_{IS} is determined by taking the average width of the stripes that correspond to G_T values within the FWHM of the peak in the histogram, as depicted in Fig. B.4. In order to compare these widths with the predictions of the reconstruction model, it is necessary to estimate the electron density gradient close to the plateau. This value can be determined from the slope of G_T near the plateau in the SGM maps. Figure B.5 illustrates our method: as discussed in section 3.3, in proximity to a plateau (Fig. B.5(a)), the electron phase is compressible and the electron density has a maximum at the QPC center (filling factor $\nu_c = G_T/G_0$). The panel (b) of Fig. B.5 shows how a reduction of the QPC width (obtained, for instance, by moving the tip toward the QPC center) is correlated to a reduction of the filling factor at the QPC center ν_c. To first order, the filling

larger than 0.41 e^2/h, so that the 1/3 peak is not observed in this scan. Also for this reason, it is convenient to plot an averaged histogram, which allows to display a larger range of G_T in a single graph.

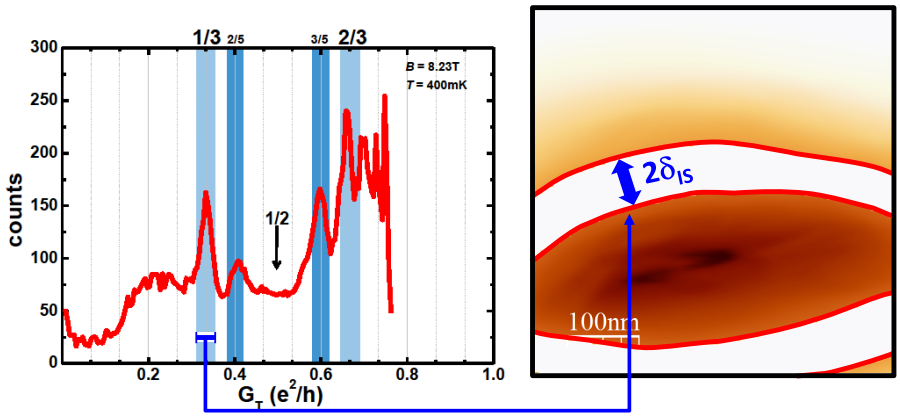

Figure B.4: The incompressible stripe width δ_{IS} is obtained starting from the FWHM of the corresponding peak in the histogram (left panel). This range of G_T values defines a circular stripe in the SGM map (right panel). δ_{IS} is given by the average width of such a stripe.

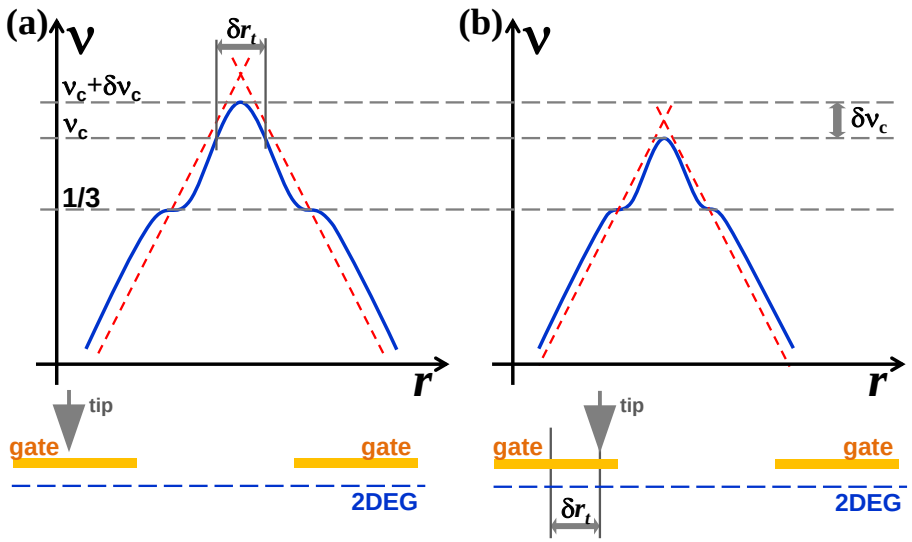

Figure B.5: (a) Local filling factor distribution within a QPC that corresponds to a tip position close to a 1/3 plateau in the SGM map. (b) A displacement δr_t of the SGM tip toward the QPC center reduces the QPC width of the same amount. The corresponding reduction of the filling factor at the QPC center (which is measured as a reduction of $G_T = \nu_c G_0$) is approximately given by $\delta r_t/2$ times the filling factor slope. Therefore we can deduce the approximate density slope directly from the G_T slope in the SGM map.

factor variation $\delta\nu_c$ at the QPC center is given by the slope of the filling factor function $\nu(r)$ times *one half* of the QPC width reduction δr_t

$$\delta\nu_c = \frac{d\nu}{dr}\frac{\delta r_t}{2}, \tag{B.1}$$

With the substitution $n = n_L\nu$ and $G_T = \nu_c G_0$, we obtain immediately Eq. 3.1

$$\frac{dn}{dr} = \frac{n_L\delta\nu_c}{\frac{1}{2}\delta r_t} = 2n_L\left(\frac{1}{G_0}\frac{\delta G_T}{\delta r_t}\right). \tag{B.2}$$

Appendix C

Nanofabrication protocols

C.1 List of samples

Here we report the list of the samples employed in this thesis. The samples were fabricated in the Clean Room of the NEST lab of the Scuola Normale Superiore, starting from the heterostructures listed in Table C.1.

- **Sample A:** Hall bar fabricated starting from the **#6_8_05.1 (a)** heterostructure, with three pairs of Schottky split-gates. The gates are patterned by thermal evaporation of a Ti/Au (10/20 nm) bilayer. The split-gate gap is 300 nm.
- **Sample B:** Hall bar fabricated starting from the **#HM2411 (a)** heterostructure, with three pairs of Schottky split-gates. The gates are patterned by thermal evaporation of a Ti/Au (10/20 nm) bilayer. The split-gate gap is 300 nm.
- **Sample C:** Hall bar fabricated starting from the **#6_8_05.1 (b)** heterostructure, with three pairs of Schottky split-gates. The gates are patterned by thermal evaporation of a Ti/Au (10/20 nm) bilayer. The split-gate gap is 400 nm.
- **Sample D:** Hall bar fabricated starting from the **#HM2417** heterostructure, with three pairs of Schottky split-gates. The gates are patterned by thermal evaporation of a Ti/Au (10/20 nm) bilayer. The split-gate gap is 300 nm.
- **Sample E:** Hall bar fabricated starting from the **#HM2411 (b)** heterostructure, with two nominally identical devices, #**E1** and #**E2**. Each device consists of three Schottky gates, which allows to implement the QH circuit of Fig. 4.1(b). The gates are patterned by thermal evaporation of a Ti/Au (10/20 nm) bilayer. The constriction defined at the device center is 1.2 μm wide and 6 μm long (thus the maximum

interaction path length for these devices is 6 μm). The gap between the selector gate (the one which sets the 2DEG filling factor at $\nu = 2$ in Fig. 4.1(b)) and the adjacent one is only 50 nm.

Sample	Heterostructure	n (cm^{-2})	μ (cm^2/Vs)	D (nm)
A	**#6_8_05.1 (a)**	1.77×10^{11}	4.6×10^{6}	80
C	**#6_8_05.1 (b)**	1.99×10^{11}	4.5×10^{6}	80
B	**#HM2411 (a)**	3.2×10^{11}	2.3×10^{6}	55
E	**#HM2411 (b)**	3.2×10^{11}	4.2×10^{6}	55
D	**#HM2417**	2.11×10^{11}	3.88×10^{6}	100

Table C.1: Details of the $Al_{0.3}Ga_{0.7}As$/GaAs heterostructures used in this thesis. We report the electron density (n) and mobility μ *in the dark* for each sample, as determined by Shubnikov-de Haas measurements, together with the 2DEG depth (D). The structures **#6_8_05.1 (a)** and **#6_8_05.1 (b)** have been obtained from the same wafer, grown by L. N. Pfeiffer and K. W. West at the Bell Laboratories Lucent Technologies, Murray Hill, NJ, USA. The differences in the sample density and mobility are due to inhomogeneity (the sample was *not* rotated during growth). Similarly the structures **#HM2411 (a)** and **#HM2411 (b)** have been obtained from the same wafer, grown without rotation. Samples **#HM2411** (**a** and **b**) and **#HM2417** have been grown by G. Biasiol and L. Sorba at the Laboratorio TASC, Basovizza (TS), Italy.

C.2 Fabrication protocols

C.2.1 Optical lithography

- Clean the sample by means of acetone, then by isopropanol to remove the acetone.
- Spin (using the UV resist S1818) at 6000 rpm for 60 s.
- Bake at 90°C for 60 s.
- Dip the sample in the developer solution (MF319) for 20 s. Stop in de-ionized water.[1]
- UV exposure for 12 s.
- Bake at 120°C for 20 s.[1]
- Dip the sample in the developer solution (MF319) for 30 s. Stop in de-ionized water.

[1] Optional surface-hardening procedure to obtain a T-shaped mask.

C.2.2 Electron-beam lithography using a bilayer mask

- Clean the sample by means of acetone, then by isopropanol in order to remove the acetone.
- Spin the co-polymer EL-13 at 6000 rpm for 90 s.
- Bake 170°C for 15 min.
- Spin the polymer A4 at 3500 rpm for 45 s.
- Bake 170°C for 15 min.
- SEM beam exposure (voltage 30 kV, working distance 10 mm, and dose of 350-500 μC/cm^2).
- Dip the sample in the developer solution (AR 600-56) for 20 s. Stop in isopropanol for 20 s.

C.2.3 Thermal evaporation and lift-off

- Load the sample in the evaporation chamber. Wait until the chamber vacuum pressure is less than $\approx 10^{-5}$ mbar.
- Evaporate in succession the metal layers (evaporation rates: 0.1-0.5 nm/s).
- Vent the chamber and unload the sample.
- Dip in acetone for at least 15 min.
- Flush with acetone by means of a syringe.
- Clean using isopropanol.

C.2.4 Wet etching

- Dip the sample in the etching solution H_3PO_4:H_2O_2:H_2O with concentration 3:1:50 for 65 s (GaAs etching rate 80 nm/min).
- Stop the etching in de-ionized water.

C.2.5 Ohmic contact annealing

- Put the sample onto the molybdenum strip in the vacuum chamber.
- Flush and pump the chamber in N_2 for 10 min.
- Set the N_2 flux to 0.5 l/min.
- Set the current supply to 12.5 A for 70 sec.
- Flush the chamber and remove the sample.

Bibliography

[1] T. D. Ladd, F. Jelezko, R. Laflamme, Y. Nakamura, C. Monroe, and J. L. O'Brien, Nature **464**, 45 (2010).

[2] D. Arovas, J. R. Schrieffer, and F. Wilczek, Phys. Rev. Lett. **53**, 722 (1984).

[3] L. P. Kouwenhoven, B. J. van Wees, N. C. van der Vaart, C. J. P. M. Harmans, C. E. Timmering, and C. T. Foxon, Phys. Rev. Lett. **64**, 685 (1990).

[4] A. M. Chang and J. E. Cunningham, Solid State Commun. **72**, 651 (1989).

[5] C. W. J. Beenakker, C. Emary, M. Kindermann, and J. L. van Velsen, Phys. Rev. Lett. **91**, 147901 (2003).

[6] Y. Ji, Y. Chung, D. Sprinzak, M. Heiblum, D. Mahalu, and H. Shtrikman, Nature **422**, 415 (2003).

[7] P. Samuelsson, E. V. Sukhorukov, and M. Büttiker, Phys. Rev. Lett. **92**, 026805 (2004).

[8] I. Neder, N. Ofek, Y. Chung, M. Heiblum, D. Mahalu, and V. Umansky, Nature **448**, 333 (2007).

[9] V. Giovannetti, F. Taddei, D. Frustaglia, and R. Fazio, Phys. Rev. B **77**, 155320 (1990).

[10] D. B. Chklovskii, B. I. Shklovskii, and L. I. Glazman, Phys. Rev. B **46**, 4026 (1992).

[11] B. I. Halperin, Phys. Rev. B **25**, 2185 (1982).

[12] S. L. Sondhi, A. Karlhede, S. A. Kivelson, and E. H. Rezayi, Phys. Rev. B **47**, 16419 (1993).

[13] H. L. Störmer, Physica B **177**, 401 (1992).

[14] H. L. Störmer, A. Chang, D. C. Tsui, J. C. M. Hwang, A. C. Gossard, and W. Wiegmann, Phys. Rev. Lett. **50**, 1953 (1983).

[15] R. B. Laughlin, Phys. Rev. Lett. **50**, 1395 (1983).

[16] S. M. Girvin, A. H. MacDonald, and P. M. Platzman, Phys. Rev. B **33**, 2481 (1986).

[17] R. de Picciotto, M. Reznikov, M. Heiblum, V. Umansky, G. Bunin, and D. Mahalu, Nature **389**, 162 (1997).

[18] F. D. M. Haldane, Phys. Rev. Lett. **51**, 605 (1983).

[19] J. K. Jain, Phys. Rev. Lett. **63**, 199 (1989).

[20] J. K. Jain, Phys. Rev. B **41**, 7653 (1990).

[21] X.-G. Wen, Phys. Rev. B **41**, 12838 (1990).

[22] X.-G. Wen, Phys. Rev. B **43**, 11025 (1991).

[23] J. M. Luttinger, J. Math. Phys. **4**, 1154 (1963).

[24] S. Roddaro, V. Pellegrini, F. Beltram, G. Biasiol, L. Sorba, R. Raimondi, and G. Vignale, Phys. Rev. Lett. **90**, 046805 (2003).

[25] S. Roddaro, V. Pellegrini, F. Beltram, G. Biasiol, and L. Sorba, Phys. Rev. Lett. **93**, 046801 (2004).

[26] S. Roddaro, V. Pellegrini, F. Beltram, L. N. Pfeiffer, and K. W. West, Phys. Rev. Lett. **95**, 156804 (2005).

[27] S. Roddaro, N. Paradiso, V. Pellegrini, G. Biasiol, L. Sorba, and F. Beltram, Phys. Rev. Lett. **103**, 016802 (2009).

[28] C. W. J. Beenakker, Phys. Rev. Lett. **64**, 216 (1990).

[29] A. M. Chang and J. E. Cunningham, Solid State Commun. **69**, 2114 (1992).

[30] I. Neder, M. Heiblum, Y. Levinson, D. Mahalu, and V. Umansky, Phys. Rev. Lett. **96**, 016804 (2006).

[31] I. Neder, F. Marquardt, M. Heiblum, D. Mahalu, and V. Umansky, Nat. Phys. **3**, 534 (2007).

[32] P. Roulleau, F. Portier, D. C. Glattli, P. Roche, A. Cavanna, G. Faini, U. Gennser, and D. Mailly, Phys. Rev. B **76**, 161309(R) (2007).

[33] F. E. Camino, W. Zhou, and V. J. Goldman, Phys. Rev. Lett. **95**, 246802 (2005).

[34] F. Marquardt and C. Bruder, Phys. Rev. Lett. **92**, 056805 (2004).

[35] C. L. Kane, Phys. Rev. Lett. **90**, 226802 (2003).

[36] K. T. Law, D. E. Feldman, and Y. Gefen, Phys. Rev. B **74**, 045319 (2006).

[37] T. Jonckheere, P. Devillard, A. Crépieux, and T. Martin, Phys. Rev. B **72**, 201305 (2005).

[38] M. J. Yoo, T. A. Fulton, H. F. Hess, R. L. Willett, L. N. Dunkleberger, R. J. Chichester, L. N. Pfeiffer, and K. W. West, Science **276**, 579 (1997).

[39] A. Yacoby, H. F. Hess, T. A. Fulton, L. N. Pfeiffer, and K. W. West, Solid State Commun. **111**, 1 (1999).

[40] N. B. Zhitenev, T. A. Fulton, A. Yacoby, H. F. Hess, L. N. Pfeiffer, and K. W. West, Nature **404**, 473 (2000).

[41] J. Martin, S. Ilani, B. Verdene, J. Smet, V. U. D. M. D. Schuh, G. Abstreiter, and A. Yacoby, Science **305**, 980 (2004).

[42] K. L. McCormick, M. T. Woodside, M. Huang, M. Wu, P. L. McEuen, C. Duruoz, and J. S. Harris-jr, Phys. Rev. B **59**, 4654 (1999).

[43] E. Ahlswede, J. Weis, K. v Klitzing, and K. Eberl, Physica E **12**, 165 (2002).

[44] G. Finkelstein, P. I. Glicofridis, R. C. Ashoori, and M. Shayegan, Science **289**, 90 (2000).

[45] G. Finkelstein, P. I. Glicofridis, S. H. Tessmer, R. C. Ashoori, and M. R. Melloch, Phys. Rev. B **61**, R16323 (2000).

[46] N. Aoki, C. R. daCunha, R. Akis, D. K. Ferry, and Y. Ochiai, Phys. Rev. B **72**, 155327 (2005).

[47] M. A. Topinka, B. J. LeRoy, S. E. J. Shaw, E. J. Heller, R. M. Westervelt, K. D. Maranowski, and A. C. Gossard, Science **289**, 2323 (2000).

[48] M. A. Topinka, B. J. LeRoy, R. M. Westervelt, S. E. J. Shaw, R. Fleischmann, E. J. Heller, K. D. Maranowski, and A. C. Gossard, Nature **410**, 183 (2001).

[49] E. J. Heller and S. E. J. Shaw, International Journal of Modern Physics B **17**, 3977 (2003).

[50] K. E. Aidala, R. E. Parrott, T. Kramer, E. J. Heller, R. M. Westervelt, M. P. Hanson, and A. C. Gossard, Nat. Phys. **3**, 464 (2007).

[51] L. P. Kouwenhoven, D. G. Austing, and S. Tarucha, Rep. Prog. Phys. **64**, 701 (2001).

[52] C. Altimiras, H. le Sueur, U. Gennser, A. Cavanna, D. Mailly, and F. Pierre, Nature Phys. **6**, 34 (2009).

[53] S. H. Tessmer, P. I. Glicofridis, R. C. Ashoori, L. S. Levitov, and M. R. Melloch, Nature **392**, 51 (1998).

[54] P. Weitz, E. Ahlswede, J. Weis, K. v Klitzing, and K. Eberl, Physica E **6**, 247 (2000).

[55] V. S. Khrapai, A. A. Shashkin, M. G. Trokina, V. T. Dolgopolov, V. Pellegrini, F. Beltram, G. Biasiol, and L. Sorba, Phys. Rev. Lett. **99**, 086802 (2008).

[56] E. V. Deviatov, A. A. Kapustin, V. T. Dolgopolov, A. Lorke, D. Reuter, and A. D. Wieck, Phys. Rev. B **74**, 073303 (2006).

[57] G. Müller, D. Weiss, A. V. Khaetskii, K. von Klitzing, S. Koch, H. Nickel, W. Schlapp, and R. Lösch, Phys. Rev. B **45**, 3932 (1992).

[58] S. Komiyama, H. Hirai, M. Ohsawa, Y. Matsuda, S. Sasa, and T. Fujii, Phys. Rev. B **45**, 11085 (1992).

[59] Y. Acremann, T. Heinzel, K. Ensslin, E. Gini, H. Melchior, and M. Holland, Phys. Rev. B **59**, 2116 (1999).

[60] A. Würtz, R. Wildfeuer, A. Lorke, E. V. Deviatov, and V. T. Dolgopolov, Phys. Rev. B **65**, 075303 (2002).

[61] T. Nakajima, Y. Kobayashi, S. Komiyama, M. Tsuboi, and T. Machida, Phys. Rev. B **81**, 085322 (2010).

[62] M. T. Woodside, C. Vale, P. L. McEuen, C. Kadow, K. D. Maranowski, and A. C. Gossard, Phys. Rev. B **64**, 041310(R) (2001).

[63] G. A. Steele, R. C. Ashoori, L. N. Pfeiffer, and K. W. West, Phys. Rev. Lett. **95**, 136804 (2005).

[64] M. Büttiker, Y. Imry, R. Landauer, and S. Pinhas, Phys. Rev. B **31**, 6207 (1985).

[65] M. Büttiker, Phys. Rev. B **38**, 9375 (1988).

[66] T. Machida, H. Hirai, S. Komiyama, T. Osada, and Y. Shiraki, Phys. Rev. B **54**,14261 (1996).

[67] K. Ikushima, H. Sakuma, S. Komiyama, and K. Hirakawa, Phys. Rev. B **76**, 165323 (2007).

[68] K. Ikushima, D. Asaoka, S. Komiyama, T. Ueda, and K. Hirakawa, Physica E **42**, 1034 (2010).

[69] S. Komiyama, H. Hirai, S. Sasa, and S. Hiyamizu, Phys. Rev. B **40**, 12566 (1989).

[70] S. Komiyama, H. Sakuma, K. Ikushima, and K. Hirakawa, Phys. Rev. B **73**, 045333 (2006).

[71] N. Paradiso, S. Heun, S. Roddaro, D. Venturelli, F. Taddei, V. Giovannetti, R. Fazio, G. Biasiol, L. Sorba, and F. Beltram, Phys. Rev. B **83**, 155305 (2011).

[72] D. B. Chklovskii, B. I. Shklovskii, and L. I. Glazman, Phys. Rev. B **46**, 15606 (1992).

[73] B. Karmakar, D. Venturelli, L. Chirolli, F. Taddei, V. Giovannetti, R. Fazio, S. Roddaro, G. Biasiol, L. Sorba, V. Pellegrini, et al., Phys. Rev. Lett. **107**, 236804 (2011).

[74] P. Roulleau, F. Portier, P. Roche, A. Cavanna, G. Faini, U. Gennser, and D. Mailly, Phys. Rev. Lett. **100**, 126802 (2008).

[75] L. V. Litvin, H. P. Tranitz, W. Wegscheider, and C. Strunk, Phys. Rev. B **75**, 033315 (2008).

[76] C. Nayak, S. H. Simon, A. Stern, M. Freedman, and S. D. Sarma, Rev. Mod. Phys. **80**, 1083 (2008).

[77] D. B. Chklovskii, K. A. Matveev, B. I. Shklovskii, and L. I. Glazman, Phys. Rev. B **47**, 12606 (1993).

Glossary

1D: One-dimensional
1DES: One-dimensional electron system
2DEG: Two-dimensional electron gas
AFM: Atomic Force Microscopy
CS: Compressible Stripe
IS: Incompressible Stripe
KPFM: Kelvin Probe Force Microscopy
LHe: Liquid Helium
LL: Landau Level
MZI: Mach-Zehnder Interferometer
QH: Quantum Hall
QPC: Quantum Point Contact
SCM: Scanning Capacitance Microscopy
SET: Single Electron Transistor
SETSE: Single Electron Transistor Scanning Electrometer
SGM: Scanning Gate Microscopy
SPM: Scanning Probe Microscopy
STM: Scanning Tunneling Microscopy
TF: Tuning Fork

Acknowledgements

I would like to express my gratitude to my advisors, prof. Fabio Beltram and dr. Stefan Heun for their confidence in my faculties. In particular, the achievement of this thesis work has been possible thanks to the patience of Stefan Heun, who helped me to solve all the practical problems related with the setup of a complex equipment as the low-temperature SGM system. I am deeply indebted to him for having taught me the basics of the AFM operation, and for the fruitful discussions that enriched our work.

A special acknowledgement goes to Stefano Roddaro, whose bright ideas played a fundamental role in the progress of this thesis. His illuminating discussions helped me to gain an insight into the physics behind the data and to get simple, but meaningful models of the observed phenomena.

I have to thank as well Giorgio Biasiol and Lucia Sorba, who grew the heterostructures and gave me important suggestions about the samples.

A big "thank you" to all the people that helped me with the fabrication process, with the low temperature measurements, with the data analysis and with all those practical issues that characterize the PhD activity. So, I express thankfulness to Giorgio De Simoni, Elia Strambini, Biswajit Karmakar, César Pascual Garcia, Daniele Ercolani, Franco Carillo, and Pasqualantonio Pingue.

During my activity at NEST, I met a number of people that enriched my daily life with their invaluable friendship. I would like to thank Ang Li, Sarah Goler, and Massimo Morandini, for the coffee-breaks, for the good chats in the office and, of course, for their sincere friendship.

At NEST friendship also means "calcetto". I cannot forget to thank all the football players of the *Techerisi Football Club* together with, of course, those people that only joined the after-match pizza.

With the achievement of the Ph.D. I must to say hello to Pisa, and to all the people that shared with me more than nine wonderful and unforgettable years. In particular, thank you to Andi and Anda (real names) and to the *Lanacaprina* group, and in particular the freshers of the Physics course 2002/2003 at the Pisa University: Ele, Esther, Giancarlo, Ietta, Oriella, and Silvia B.

A special acknowledgement goes to my best friend Francesco, for his fundamental support during the hard periods, and for the adventures he

dragged me into.

Finally, I express my gratitude to my family and in particular to my brother Marco and my sister Giulia, to whom this thesis is dedicated.